Benedikt Schönhuber, BSc

Measurement of Residual Stress in Cemented Carbides Using Electron Backscatter Diffraction

Master's Thesis

to achieve the university degree of

Diplom-Ingenieur

Master's degree program: Technical Physics

submitted to

Graz University of Technology

Supervisor
Ao.Univ.-Prof. Dipl-Ing. Dr.techn. Werner Grogger

Co-Supervisor
Dipl-Ing. Dr.techn. Stefan Mitsche

Institute of Electron Microscopy and Nanoanalysis

Graz, October 2020

Affidavit

I declare that I have authored this thesis independently, that I have not used other than the declared sources/resources, and that I have explicitly indicated all material, which has been quoted either literally or by content from the sources used. The text document uploaded to TUGRAZonline is identical to the present master's thesis.

28.10.2020

Date

Schönhuber Benedikt

Signature

Abstract

For the production of better and more resistant work pieces from cemented carbides, it is important to understand the influence of the manufacturing process on the properties of the work piece. One property with a big influence on the quality of the work piece is residual stress. To investigate residual stress levels, many methods are available and well-established. Electron backscatter diffraction (EBSD) in combination with the commercially available CrossCourt 4.0 (CC4) software is one of these methods. The aim of this present work is to evaluate the possibilities and reliability of the values obtained by the CC4 software and to investigate the influence of surface treatment on stress levels in carbide metals. EBSD in combination with the CC4 software is a versatile tool to locate and characterise type III stress on a microscopic level. The examination via EBSD and CC4 uses cross correlation functions (XCFs) to analyse Kikuchi patterns, originating from the backscattered electrons (BSEs). This thesis starts with the investigation of a silicon (Si) single crystal wafer to characterise its stress levels to get an insight into the functionality and precision of the values of the CC4 software. Cemented carbide samples were ground on the surface and residual stress levels were examined. A comparison of the obtained values and values from the well-established x-ray diffraction (XRD) method together with values from the literature was done. Besides the assumption of low stress levels within the Si wafer, a σ_{11} evaluation resulted in values between $-70\ MPa$ and $60\ MPa$. Four types of cemented carbides were examined differing in their magnetic saturation, high or low, and concerning their surface, either ground or untreated. Within these samples a dependence between surface treatment and residual stress levels at the surface could be shown. The residual stress is present within tungsten-carbide (WC) grains, cobalt (Co) grains release high residual stress levels via a phase transition from face centered cubic (fcc) to hexagonal closed pack (hcp). The Co binder phase consists of grains, larger than the examined areas of $20x20\ \mu m^2$. Comparing the obtained values is complicated, due to the different stress types measured by the XRD and EBSD method. This thesis shows in particular the advantages and disadvantages of residual stress analysis using EBSD method together with the CC4 software.

Kurzfassung

Für bessere und widerstandsfähigere Hartmetallbauteile ist es unerlässlich, den Einfluss des Produktionsprozesses auf die Eigenschaften des Bauteils zu kennen. Eine Eigenschaft, die großen Einfluss auf die Qualität der Werkstücke hat, ist die Eigenspannung. Um diese zu untersuchen, sind viele Methoden verfügbar und gut etabliert. Eine mögliche Methode ist, Elektronenrückstreubeugung EBSD in Kombination mit der kommerziell verfügbaren CrossCourt 4.0 (CC4) Software. Diese Arbeit untersucht die Möglichkeiten und Zuverlässigkeit der Ergebnisse der CC4 Software und wertet den Einfluss von Schleifprozessen an der Oberfläche auf die mechanische Eigenspannung in Hartmetallen aus. Electron backscatter diffraction (EBSD) in Kombination mit der CC4 Software ist ein vielseitiges Werkzeug, um mechanische Eigenspannungen dritter Art auf einem mikroskopischen Level zu lokalisieren und charakterisieren. Untersuchungen durch EBSD und CC4 verwenden Kreuzkorrelationsfunktionen XCF um Kikuchi-Muster auszuwerten, die durch Rückstreuelektronen entstehen. Zu Beginn wurde ein Silizium Einkristall Wafer untersucht und bezüglich seiner mechanischen Eigenspannungwserte charakterisiert, um einen Einblick in die Funktionsweise und Genauigkeit der Werte der CC4 Software zu bekommen. Im Weiteren wurden Hartmetall-Werkstücke an der Oberfläche geschliffen und die Eigenspannungwerte untersucht. Die erhaltenen Werte wurden dann mit Werten der etablierten Röntgenbeugung XRD Eigenspannungsmessmethode und Werten aus der Literatur verglichen. Für den Silizium-Einkristall-Wafer wurden, trotz der Annahme eines weitgehend eigenspannungsfreien Kristalls, σ_{11} Eigenspannungswerte zwischen -70 MPa und 60 MPa gefunden. Es wurden vier verschiedene Hartmetall-Grobkornproben untersucht mit hoher und tiefer magnetischer Sättigung und mit geschliffener Oberfläche und sinterroh. In diesen Wolframkarbid-Kobalt WC-Co Hartmetallen konnte gezeigt werden, dass durch Oberflächenbehandlung mechanische Verspannungen entstehen und bezüglich der Tiefe auf eine Korngröße begrenzt sind. Die Eigenspannungen sind in den Wolframkarbid (WC) Körnern lokalisiert, die Kobalt (Co) Körner bauen hohe mechanische Eigenspannung über eine Phasentransformation von einem flächenzentriert kubischem Gitter fcc zu einem Gitter mit hexagonal dichtester Kugel-

packung hcp ab. Die Binderphase bildet Körner aus, die weit größer als die betrachteten Gebiete von $20x20$ μm^2 sind. Ein Vergleich der gemessenen Eigenspannungswerte gestaltete sich unter anderem aufgrund der unterschiedlichen gemessenen Eigenspannungspannungsarten der Messmethoden x-ray diffraction (XRD) und EBSD als schwierig. Diese Arbeit zeigt detailliert die Stärken und Schwächen von Eigenspannungsanalysen mittels EBSD und der CC4 Software.

Acknowledgements

I wish to express my gratitude to all the people who helped in one way or another to realise this work and supported me throughout the course of this thesis.

First of all I want to thank Professor Ferdinand Hofer and Professor Gerald Kothleitner for giving me the opportunity to write my thesis at the FELMI-ZFE.

I want to thank especially Professor Werner Grogger for his continuous scientific support. His encouraging feedback sharpened my approaches, and brought a higher level to my work.

I am especially grateful for the guidance and help of Dr Stefan Mitsche who encouraged me whenever necessary. In countless discussions, he guided me, also out of every dead-end, along the road.

I am extremely thankful for the help of Martina Dienstleder. She was always present with helpful advice when questions concerning the preparation of experimental samples came up.

For their subject-specific help, I want to express my gratitude to Dr Ralph Useldinger and Marianne Penoy from CERATIZIT Luxembourg S.à r.l.

A special thank goes to all the members of the FELMI-ZFE institute for discussions and help concerning my thesis, but also for the warm and welcoming atmosphere at the institute.

My appreciation also extends to the Aluminum Crew, my colleagues throughout the time I worked on my thesis. For the wonderful "Diplomandenabende" and the atmosphere in the "Diplomandenzimmer". I want to thank Jakob, Kristina, Alexander, Daniel, Eva, Michael, Moritz, Nico, Verena, Anas and Michele.

I also want to express my gratitude to my partner Julia for her cheerful company especially within the last few months.

Finally, I would like to acknowledge with gratitude the patience and support of my parents, Michael and Christine and brothers, Paul and Florian.

Contents

Abstract v

1 Motivation and Objective 1
- 1.1 Structure . . . 2

2 Introduction 3
- 2.1 Scanning Electron Microscope . . . 3
  - 2.1.1 Electron Backscatter Diffraction . . . 6
- 2.2 Stress Basics . . . 11
  - 2.2.1 Stress Tensor . . . 11
  - 2.2.2 Elasticity . . . 11
  - 2.2.3 Residual Stress . . . 12
  - 2.2.4 Von Mises Stress . . . 14
  - 2.2.5 Stress Measurement . . . 15
  - 2.2.6 Stress Evaluation by CrossCourt 4.0 Software . . . 16
- 2.3 Tungsten Carbide . . . 17
  - 2.3.1 Sintering . . . 17
  - 2.3.2 Magnetic Saturation . . . 18

3 Experimental Procedure 19
- 3.1 Surface Treatment . . . 20
  - 3.1.1 Grinding Process . . . 20
- 3.2 Sample Preparation . . . 21
  - 3.2.1 Ion Polishing . . . 22
- 3.3 Scanning Electron Microscope . . . 24
- 3.4 OIM Data Collection . . . 24
  - 3.4.1 OIM Data Collection Settings . . . 24
- 3.5 CC4 Software . . . 26
  - 3.5.1 Elastic Coefficients . . . 27

3.5.2 CC4 Calibration of Effective Pixel Size 27
3.5.3 Data Filtering for Reference Pattern 36
3.5.4 Fast Fourier Transformation 37
3.5.5 Matlab Evaluation 41

4 Measurements and Results **44**
4.1 Calibration Measurements 45
4.1.1 Silicon Wafer Measurements 45
4.2 tungsten-carbide cobalt (WC-Co) Samples 46
4.2.1 Results of the cobalt (Co) phase (influence of the magnetic saturation and stress on the Co phase) . . 54
4.2.2 Results of the tungsten-carbide (WC) phase (influence of the grinding processes on the stress levels directly at the surface) 56
4.2.3 Residual Stress Evaluation via XRD 59

5 Discussion **60**
5.1 Preliminary Considerations 60
5.1.1 Silicon Wafer 60
5.1.2 Influence of Grooves on the Surface 64
5.1.3 Measurement Uncertainty and Absolute Values . . 64
5.2 Residual Stress Evaluation Within the Co Phase of a WC-Co sample 68
5.2.1 Sample With High Magnetic Saturation 68
5.2.2 Sample With Low Magnetic Saturation 69
5.2.3 Bulk Cross Section 70
5.3 Residual Stress Evaluation Within the WC Phase of a WC-Co sample 71
5.3.1 Sample With High Magnetic Saturation 72
5.3.2 Sample With Low Magnetic Saturation 72
5.3.3 Bulk Cross Section 73
5.4 Comparison of XRD and EBSD Measurements 75
5.4.1 Difficulties Comparing XRD and EBSD Values . . . 75
5.5 Overview Over the Obtained Values and Estimation of Their Reliability 76

6 Conclusion and Outlook **79**
6.1 Summary and Conclusion 79
6.2 Outlook 80
6.2.1 Preparation 80
6.2.2 Comparison between XRD and EBSD Measurements 80
6.2.3 Absolute Values 81

References **83**

List of Figures

2.1 Zeiss Ultra 55 scanning electron microscope (SEM) 4
2.2 Simulation of the electron-solid interaction in a 70° tilted case. 10000 trajectories were simulated with an electron energy of 20 keV. The simulation was done with CASINO 2.42 software. [3] 5
2.3 Geometrical principle of the capture Kikuchi pattern via EBSD 7
2.4 Principle of EBSD crystal orientation mapping 8
2.5 Comparison of Kikuchi patterns with low and high stress levels [13] 9
2.6 Influence of the bending of the crystal on the Kikuchi pattern 9
2.7 Influence of a subgrain boundary and surface preparation on the Kikuchi pattern [13] 10
2.8 Unstrained and strained lattice and their influence on the Kikuchi pattern 10
2.9 Directions of the elements of the stress tensor 11
2.10 Types of residual stress 14
2.11 Allocation of the ROIs 17
2.12 Image of cemented carbide work pieces [31] 18

3.1 Diagram of the experimental process used in this thesis . 20
3.2 Sketch of a sample glued to a blade from the Ilion™"Precision Cross-Section System Owner's Manual and User's Guide". 22
3.3 secondary electron (SE) images of a WC-Co sample with low magnetic saturation and ground surface 23
3.4 Sketch of the investigated cross sections 25
3.5 Model of the investigated surfaces of the sample 26
3.6 Diagram of the CC4 software 28

3.7 Sketches of the beam mechanics and the position of the pattern centre. The pattern centre is indicated in both images with pc. The pattern centre is obtained by laying a straight line through the incident point of the electron beam on the sample, normal to the phosphor screen. . . . 30
3.8 Sketch of the shifts in x- and y-direction 31
3.9 Representation of the pixel shifts identified on the phosphor screen by cross correlation function (XCF) versus the shift of the primary electron (PE) beam. The graphs show the shifts with and without beam shift correction. 34
3.10 σ_{VM} stress maps for a silicon wafer calculated with and without beam shift correction. The black squares in the middle of the stress maps indicate the position of the reference pattern. 35
3.11 Stress profile of a $200x200$ μm^2 area of an silicon (Si) wafer with and without beam shift calibration. The variation from linearity is assumed to originate from residual stress within the Si wafer. 36
3.12 Comparison of two different settings for defining the reference patterns for the evaluation of the WC phase of a surface cross section of a sample with high magnetic saturation and ground surface. 38
3.13 Comparison of the two different FFT settings for the evaluation of the WC phase of a surface cross section of a sample with high magnetic saturation and ground surface. 39
3.14 Stress depth profile within the WC phase of a WC-Co sample of a surface cross section of a sample with high magnetic saturation and ground surface. 41
3.15 Sketch of the calculation of the mean stress profile 42

4.1 σ_{VM} stress maps for a silicon wafer calculated with and without beam shift correction 45
4.2 Surface cross section of a sample with high magnetic saturation and untreated surface 48
4.3 Surface cross section of a sample with high magnetic saturation and ground surface 49

4.4 Surface cross section of a sample with low magnetic saturation and untreated surface 50
4.5 Surface cross section of a sample with low magnetic saturation and ground surface 51
4.6 Bulk cross section of a sample with low magnetic saturation 52
4.7 Bulk cross section of a sample with high magnetic saturation 53

5.1 Stress values of a $1x1$ mm^2 area of a silicon wafer. 62
5.2 Stress values of a $160x160$ μm^2 area of a silicon wafer. The corresponding stress maps are displayed again. The stress profile and the horizontal line are calculated for a section of $160x160$ μm^2 from the centre of the measurement. . . . 63
5.3 Mean σ_{VM} stress of the grains 67
5.4 Co stress depth profile of a surface cross section of sample with high magnetic saturation 69
5.5 Stress depth profile for Co of a surface cross section of sample with low magnetic saturation 70
5.6 Co stress profile of a bulk cross section 71
5.7 Stress depth profile for WC of a surface cross section of sample with high magnetic saturation 72
5.8 Stress depth profile for WC of a surface cross section of sample with low magnetic saturation 73
5.9 Stress profile for WC of a bulk cross section 74

Abbreviations

Ar argon
BSE backscattered electron
C carbon
CCD charge coupled device
CC4 CrossCourt 4.0
CI confidence index
Co cobalt
EBSD electron backscatter diffraction
fcc face centered cubic
FE finite elements
FFT fast Fourier transformation
hcp hexagonal closed pack
HF high frequency
IPF inverse pole figure
IQ image quality
KAM kernel average misorientation
LF low frequency
OIM orientation imaging microscopy
PE primary electron

ROI region of interest
sc simple cubic
SE secondary electron
SEM scanning electron microscope
Si silicon
Ti titanium
W tungsten
WC tungsten-carbide
WC-Co tungsten-carbide cobalt
XCF cross correlation function
XRD x-ray diffraction

1 Motivation and Objective

Cemented carbides have a large number of applications across all sorts of industries. They play an important role as a material used for drills, stamps and mainly cutting tools. Tungsten-carbide cobalt (WC-Co) is a widely used alloy consisting of tungsten-carbide (WC), a hard, brittle carbide, embedded in cobalt (Co), a ductile binder phase. To manufacture cemented carbides the WC and Co powder is sintered. After the sinter process, the work piece is ground to its final shape. The sinter process and the grinding process are sources of residual stress occurring within the cemented carbides. Especially the grinding process leads to residual stress near the surface of the sample. Stress plays an important role on how a cemented carbide work piece is able to withstand utilization.

High demands on cemented carbides in terms of reliability and durability increase the need to optimize the manufacturing process and understand the impact of the process on the work piece. To meet these requirements, a better understanding of the residual stress introduced into the sample by the manufacturing process is crucial. Stress measurements can be carried out by various methods, such as hole drilling, analysing stress related changes in elastic waves or velocity variations in magnetic domains, raman spectroscopy or diffraction methods with different beam sources such as electrons, neutrons or x-rays [1]. Analyses on nano scale are necessary to provide better understanding of the stress introduced into the metal by grinding. Faster, more precise and simpler methods for analyses are crucial for further optimization of the material.

With increasing camera speed electron backscatter diffraction (EBSD) has become more important within material science. EBSD represents a powerful method to analyse crystal structure and orientation on a microscopic level. Current resolutions of around *50 nm* offer the possibility to

analyse orientation changes within single grains without destruction of the sample.

This thesis examines the possibilities and reliability of EBSD methods in combination with the CrossCourt 4.0 (CC4) software for stress measurements in cemented carbides and analyses the influence of magnetic saturation and grinding processes on stress levels within WC-Co samples. Within this work, silicon (Si) single crystal wafer and WC-Co samples with high and with low magnetic saturation were examined.

1.1 Structure

This thesis presents in chapter 2 the theoretical background, EBSD basics and important material properties necessary for the evaluation of the influence of surface treatment on stress levels. The experimental procedure (chapter 3) explains the modus operandi for the preparations and measurements. There are three main parts of measurement procedures. Some samples did undergo a surface manipulation in form of a grinding process. All surfaces were prepared and measurements were executed with a scanning electron microscope (SEM). Chapter 4 describes the measurement results. These results are discussed in chapter 5. The discussion evaluates the possibilities and reliability of the CC4 software and presents the perceptions from the EBSD examinations of samples with treated and untreated surface and the influence of surface treatment on the residual stress levels of the material. A summary and outlook (chapter 6) concludes this thesis.

2 Introduction

2.1 Scanning Electron Microscope

An SEM is an instrument used for imaging on a nanoscale. Figure 2.1 shows the used Zeiss Ultra 55 [2] SEM. In an SEM a very finely focused electron beam probes the surface of the sample and excites signals originating from the interaction of the electrons with the sample. The main signals used in an SEM are the secondary and the backscattered electrons. Along their trajectories defined by collisions with nuclei and outer shell electrons, primary electron (PE) interact with the material and create secondary electrons (SEs), backscattered electrons (BSEs) and other signals. SEs are outer shell electrons of the atoms and are used to obtain an image of the surface of the sample. Besides other applications BSEs are used for EBSD and therefore mainly evaluated in this thesis. These electrons are PEs scattered back out of the sample. As they undergo a scattering process with the atomic nuclei, the number of BSEs depends on the atomic number of the scattering atom. For EBSD evaluations they are detected by a phosphorous screen and captured by a charge coupled device (CCD) camera.

The spatial resolution is limited by the electron-solid interaction. The volume of the electron-solid interaction is simulated in figure 2.2. Figure 2.2a shows a Monte Carlo simulation of the trajectories of electrons inside a tilted sample. Most of the BSE trajectories escape within a radius of about 500 nm (figure 2.2b). The simulation prompts that a region with a high density of BSEs at an energy of 20 keV lies within a radius of about 70 nm. For the analysis of WC-Co samples, which will be explained later, a step size of 100 nm to 200 nm showed to be useful.

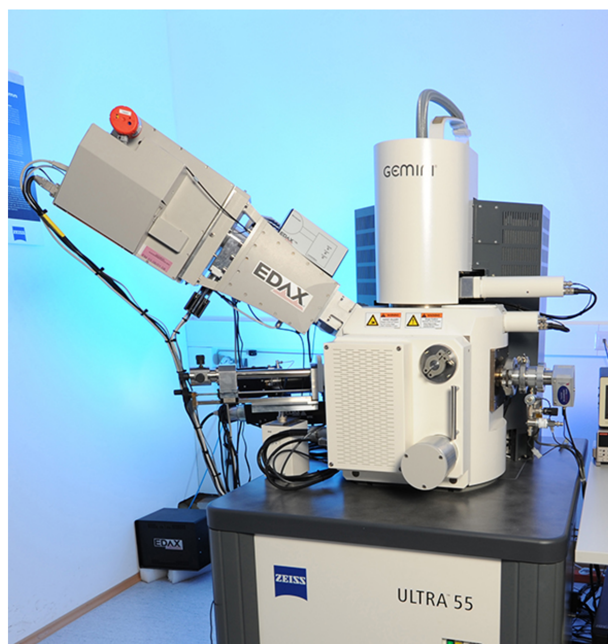

Figure 2.1: Zeiss Ultra 55 SEM

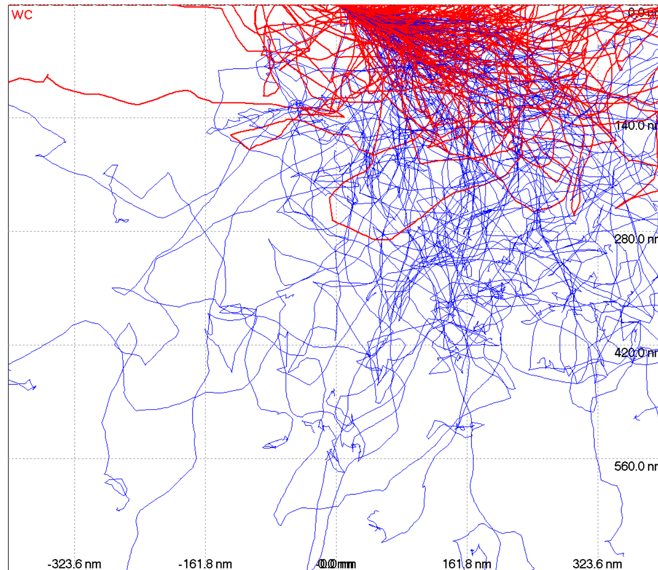

(a) Trajectories of electrons inside a 70° tilted sample. BSEs are indicated red. The blue trajectories are electrons terminated within the sample.

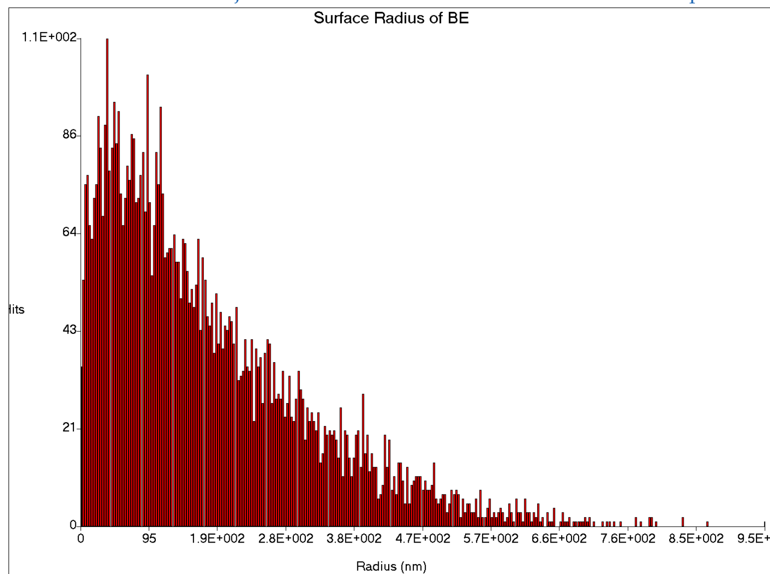

(b) Distance from the point of penetration and the point of escape of BSE.

Figure 2.2: Simulation of the electron-solid interaction in a 70° tilted case. 10000 trajectories were simulated with an electron energy of 20 keV. The simulation was done with CASINO 2.42 software. [3]

2.1.1 Electron Backscatter Diffraction

EBSD is a powerful method for mapping crystal orientations over a large area [4]. It is based on the capture of diffraction patterns on a phosphor screen. As demonstrated in figure 2.3, the electron beam hits the strongly tilted sample and gets scattered inelastically within the sample. The electrons are now moving diffusely within the sample in every direction. These diffuse electrons are reflected and scattered by atoms of the lattice planes. The diffuse directions of the electron paths provide every lattice plane with suitable electrons with the necessary Θ angle for the Bragg equation 2.1. The backscattered electrons form Kossel cones and are made visible on the phosphor screen as Kikuchi lines [5]. All Kikuchi lines captured by the phosphor screen for one position form the Kikuchi pattern, which is therefore containing angular relationships of a crystal, interzonal and interplanar angles [6]. The angles between the plane presented by the Kikuchi band leads to the interplanar angles, and since the angular width of such a Band is twice the Bragg angle Θ, the width of the Kikuchi bands corresponds to the interplanar spacing [7].

$$n\lambda = 2d\, sin(\Theta) \tag{2.1}$$

n	refraction index (1 in vacuum)
λ	wavelength of the imaging radiation
d	distance between the lattice planes
Θ	angle between the incident beam and the lattice plane

A high speed CCD from Thorlabs scientific [9] captures the patterns. With the Bragg equation, the distance between the lattice planes can be calculated, and with the distance between the lattice planes, every Kikuchi line can be assigned to a certain lattice plane, when material and phase are known. From the orientation and position of the Kikuchi lines in combination with the pattern center, the software is able to obtain the orientation of the crystal by comparing it to a crystallographic database. The pattern center is obtained by taking a line orthogonal to the phosphor screen through the point where the incident electron beam

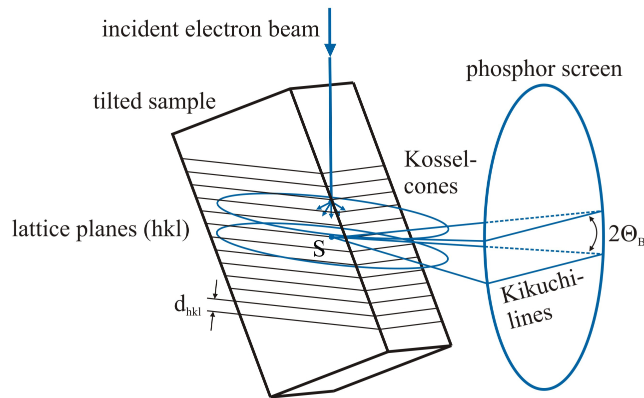

Figure 2.3: Geometrical principle of the generation of Kikuchi patterns via EBSD taken from Dresbach et al. [8]

hits the sample. Therefore the pattern center is fixed on the phosphor screen when the phosphor screen is moved in or out. A sketch of the pattern center is shown in figure 3.7b. The comparison of the obtained Kikuchi pattern with the database is done automatically by OIM Data collection V7.3 [10] software analysing the Kikuchi lines [11]. Figure 2.4a demonstrates the working principle of EBSD. The orientation of the crystals at all scanning points is presented as an inverse pole figure (IPF). Each colour indices a certain orientation. The association of colour and orientation is realised via the Miller indices or $h, k, l - planes$. In figure 2.4b the Kikuchi pattern of an Si single crystal with diamond cubic structure is displayed.

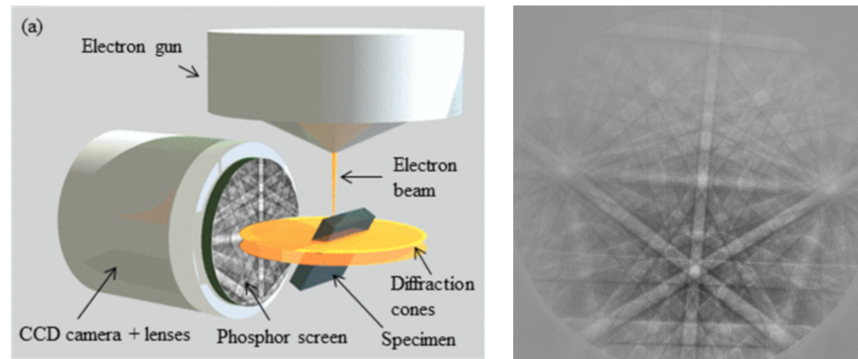

(a) Capture of a Kikuchi pattern taken from Vespucci et al. [12]

(b) Kikuchi pattern of a silicon single crystal with diamond cubic structure, captured by the author.

Figure 2.4: Principle of EBSD crystal orientation mapping

The explanations and images of the influence of stress on the Kikuchi pattern is based on the paper "On the formation mechanisms, spatial resolution and intensity of backscatter Kikuchi patterns" by S. Zaefferer [11] and on the review "A Review of Strain Analysis Using Electron Backscatter Diffraction" by S. Wright et al. [13]. Different forms of stress and deformation result in different types of blurred and altered Kikuchi patterns. Figure 2.5a shows a reference pattern from a region with low deformation. The lines are sharp and there is no obvious stretching of the pattern. Figure 2.5b demonstrates a blurred pattern from a region with higher stress values, especially in the lower part of the image distortions are visible.

Different deformations of the Kikuchi patterns were observed during this present work. Based on figures from Wright et al. [13] possible origins of these effects are given. A common deformation was a blurring of the patterns at different positions such as the grain boundaries. This could be a result of bent and changing crystal planes as well as plane distances. A bent crystal blurs out the Kikuchi patterns as demonstrated in figure 2.6. The same effect can be seen in measurements of samples with bad surface preparation as shown in figure 2.7b. Another observed variation of the pattern is a rotation. Rotated crystals result in rotated Kikuchi patterns. Figure 2.7a demonstrates the results of rotated crystal in a combination

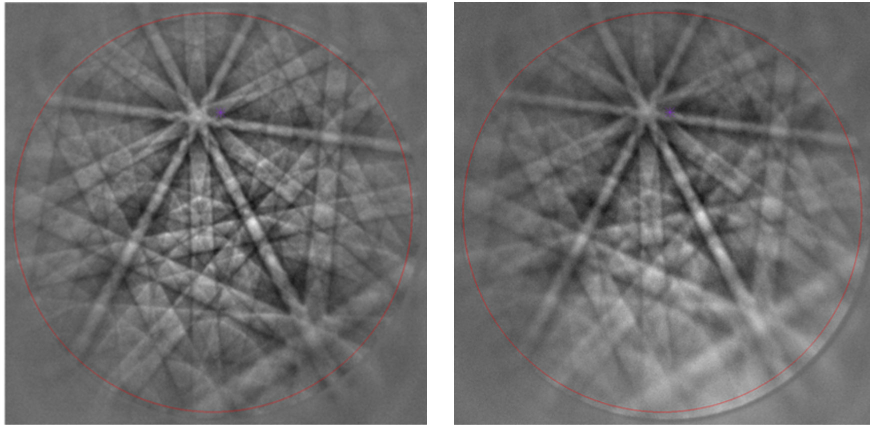

(a) Kikuchi pattern from a region with low deformation and stress (b) Kikuchi pattern from a region with high deformation and stress

Figure 2.5: Comparison of Kikuchi patterns with low and high stress levels [13]

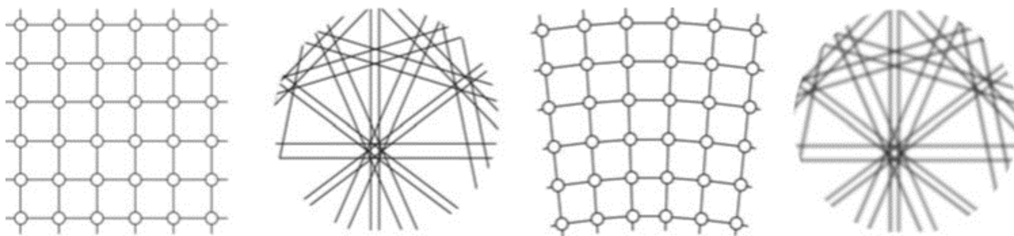

Figure 2.6: Influence of the bending of the crystal on the Kikuchi pattern. The left crystal is a perfect crystal with sharp Kikuchi lines. The left crystal is bent and therefore the Kikuchi lines are blurred. [13]

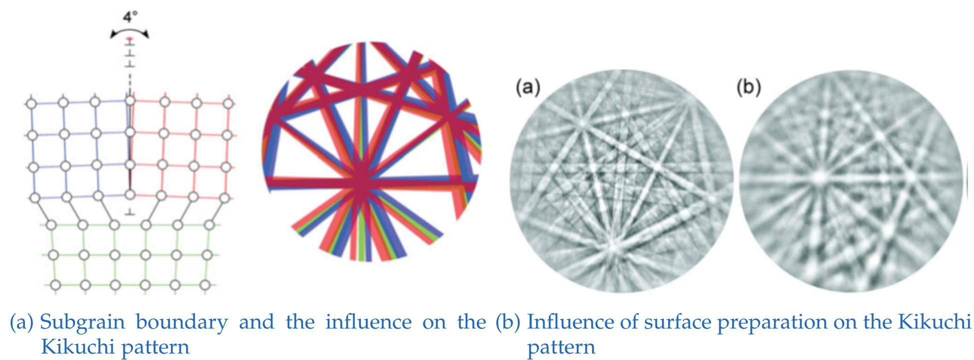

(a) Subgrain boundary and the influence on the Kikuchi pattern

(b) Influence of surface preparation on the Kikuchi pattern

Figure 2.7: Influence of a subgrain boundary and surface preparation on the Kikuchi pattern [13]

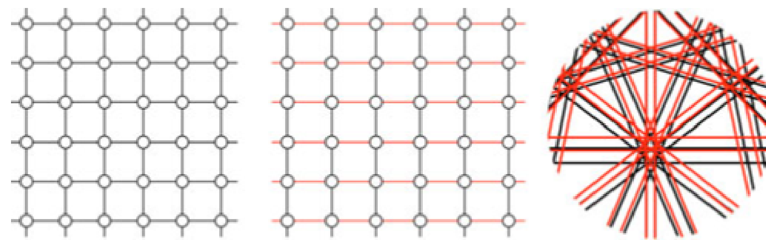

Figure 2.8: Unstrained and strained lattice and their influence on the Kikuchi pattern [13]

with a subgrain boundary. A superposition of multiple patterns can occur as demonstrated in this figure. Movement of the patterns could also be observed. This could originate either in the mechanics of the incident beam or combined with other stress related effects mentioned above. The influence of the beam mechanics is overcome by the calibration of the effective pixel size in section 3.5.2. An observed strained crystal (figure 2.8) results in stretched patterns.

2.2 Stress Basics

2.2.1 Stress Tensor

Stress as a directed quantity is measured in all spatial directions and is represented as a tensor of 2nd order. The directions are sketched in figure 2.9.

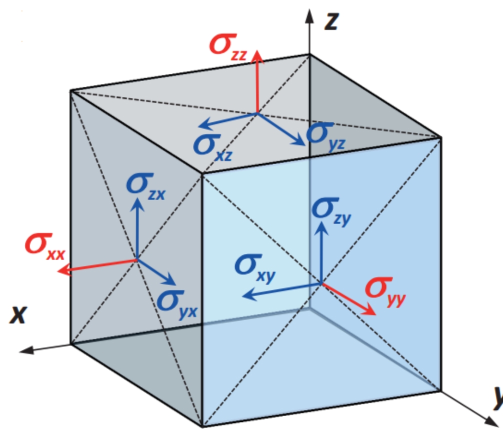

Figure 2.9: Directions of the elements of the stress tensor [14]

2.2.2 Elasticity

The values for the stress are calculated on the basis of Hooke's law, equation 2.2. Since the elasticity can be anisotropic depending on the material, the Young's modulus has to be replaced by the elasticity tensor. This tensor gives the elasticity in different directions and is different for each crystal lattice and material. The values of the tensor are known for most common materials and are underlying several restrictions, depending on the crystal lattice. To give an example, the simplest elasticity tensor is found for simple cubic (sc) crystals, where $c_{11} = c_{22} = c_{33}$,

$$\sigma = E * \epsilon \tag{2.2}$$

[15]

σ	stress
E	Young's modulus
ϵ	strain

$c_{12} = c_{13} = c_{23} = c_{21} = c_{31} = c_{32}$ and $c_{44} = c_{55} = c_{66}$ [14]. The elasticity tensor for a sc crystal can be seen in equation 2.3. The elasticity tensor is one of the inputs the CC4 software needs for calculations. Since the values are known for most standard materials, in this thesis these values were taken from the preset values of the CC4 software.

$$[c] = \begin{pmatrix} c_{11} & c_{12} & c_{12} & 0 & 0 & 0 \\ c_{12} & c_{11} & c_{12} & 0 & 0 & 0 \\ c_{12} & c_{12} & c_{11} & 0 & 0 & 0 \\ 0 & 0 & 0 & c_{44} & 0 & 0 \\ 0 & 0 & 0 & 0 & c_{44} & 0 \\ 0 & 0 & 0 & 0 & 0 & c_{44} \end{pmatrix} \tag{2.3}$$

[14]

2.2.3 Residual Stress

In "Kloos: Eigenspannungen, Definition und Entstehungsursachen" [16] residual stress is defined as static effective stress on multiple axes in a closed system, existing without moments and forces in a mechanic equilibrium. Residual stress can be classified as type one, type two and type three stress. In figure 2.10 different residual stress types are sketched and related to the belonging areas. The upper graph of the sketch shows the stress levels of the grains sketched in the lower graph. Stress over

different regions leads to different stress types. Within the sketch type I, type II and type III stress is indicated as σ_I, σ_{II} and σ_{III}.

According to Wolfstieg and Macherauch the stress types can be described by the following: Averaged over several grains stress is referred to as type I stress. Interfering with the momentum and force equilibrium results in changes of macroscopic dimensions [17]. This type of stress is evaluated by x-ray diffraction (XRD) measurements [1] [18].

Type II stress is nearly homogeneous over single grains or grain areas. Changing forces or momenta within these areas do not change macroscopic dimensions.

Type III stress is inhomogeneous over several atomic distances. Due to a high, local resolution of these type III stress values the used EBSD analysis method is required.

If type II stress is known, or the reference pattern chosen by the software is taken from a region without residual stress, it is possible to calculate the corresponding type I stress value. At the present state of the art, it is not possible to obtain patterns without residual stress or to evaluate the type II stress values. Caused by these problems in this kind of evaluation, a calculation of type I stress is not possible. This leads to one of the problems concerning the comparability of XRD and EBSD values, since XRD measures type I stress values.

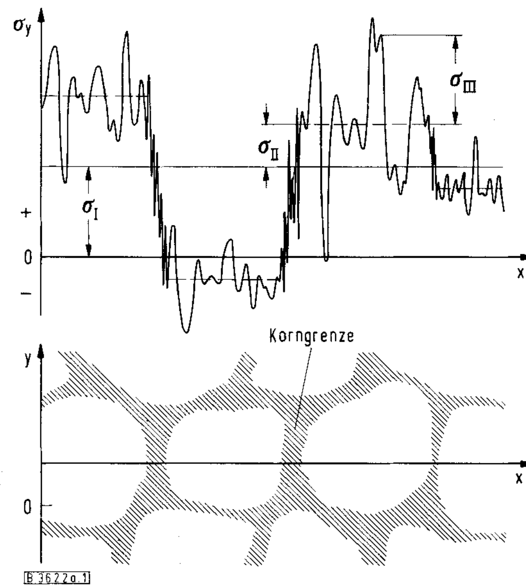

Figure 2.10: Types of residual stress. Taken from Wolfstieg and Macherauch [17].

2.2.4 Von Mises Stress

The von Mises stress is a scalar value calculated from the stress tensor. It combines the tensor in one non-directional value, which means that the directions of the stress values in the stress tensor are lost. The von Mises stress is calculated after equation 2.4. In this thesis the calculation is executed without the author's intervention by the CC4 software. Directly connected to the von Mises stress is the von Mises yield criterion which gives the maximum von Mises stress value, the yield strength, for ductile materials before yielding takes place [15]. Cardarelli [19] states the ultimate tensile strength (yield strength) for WC with 344 MPa. Zhu et al. [20] could show in a simulation that the von Mises stress in the WC phase of a WC-Co with 10% Co could get as high as 9026 MPa.

$$\sigma_{VM} = \sqrt{\frac{1}{2}\left[(\sigma_{11}-\sigma_{22})^2+(\sigma_{22}-\sigma_{33})^2+(\sigma_{11}-\sigma_{33})^2\right]+3(\sigma_{12}^2+\sigma_{23}^2+\sigma_{13}^2)} \tag{2.4}$$

[15]

σ_{VM}	von Mises stress
σ_{xx}	elements of the stress tensor (x can either be 1,2 or 3)

2.2.5 Stress Measurement

Increasingly high demands on work pieces and materials require profound understanding of manufacturing processes and their influence on material properties. Especially hard metals are expected to withstand high pressure applications as well as severe impact from all sorts of treatment and utilization. Stress introduced through application is one of the possible stress sources, however, within the material so-called residual stress is present without using the work piece.

The measurement method for residual stress is chosen depending on the stress type of interest. These methods are divided into destructive and non-destructive measurement techniques. Destructive techniques are based on the removal of material and thereby relieving the stress, for example hole drilling and layer removal. With these methods stress is measured indirectly via strain measurements [21].

Non-destructive methods are mostly centred around diffraction, such as neutron diffraction or XRD, and evaluate the strains of specific lattice planes of the crystal. All of these methods are suitable for type-I stress measurements due to limitations of the x-rays' or neutron beam's spatial resolution [22].

Type - II stress is measurable with the method of Raman fluorescence spectroscopy by analysing Raman peak shifts [1][23].

In this Master's thesis type-III stress in cemented carbides is measured

with EBSD. EBSD offers the possibility to analyse subgrain residual stress based on the analysis of Kikuchi patterns [24], in the case of the CC4 software via cross correlation function (XCF), as indicated in section 2.2.6 below. This method has a spatial resolution of several tens of nanometres and the used BSEs a penetration depth of around 100 nm at an acceleration voltage of 20 kV.

In an XRD analysis, x-rays are beamed onto the sample and scattered back to a detector. Depending on the orientation and distances defined by the lattice planes, there are several angles with intensity peaks. In a known material the position and width of these peaks in the diffractogram are known and residual stress can be calculated from the measured variations. A. Steuwer et al. [25] reached a spatial resolution of about 400 μm for high-resolution strain mapping. Simulations calculated the penetration depth of x-rays into WC-Co to about 3 μm.

2.2.6 Stress Evaluation by CrossCourt 4.0 Software

The CrossCourt 4.0, used in this work to determine residual stress, analyses the Kikuchi patterns of a grain relative to a reference pattern. The reference pattern is chosen by the CC4 software as the pattern of the grain with the lowest kernel average misorientation (KAM) value. Relative changes in the patterns, caused by distortions in the lattice, are calculated via XCF [26][27]. The XCF compares the similarity of two images, in this case of two Kikuchi patterns. Two very similar patterns have a high correlation and a low stress level, whereas two very different patterns have a low correlation and a high relative stress level. The XCF is utilized by splitting the Kikuchi pattern of each point into several rectangular region of interests (ROIs) as demonstrated in figure 2.11. Depending on the pattern size, mostly 20 ROIs are set. The ROIs of each pattern are compared to the corresponding reference pattern. The XCF gives a value for their similarity via picture-to-picture comparison. All the similarity values of the ROIs of a pattern in combination with the pattern center values and the sample to screen distance from the collected data of the orientation imaging microscopy (OIM) software, are used to

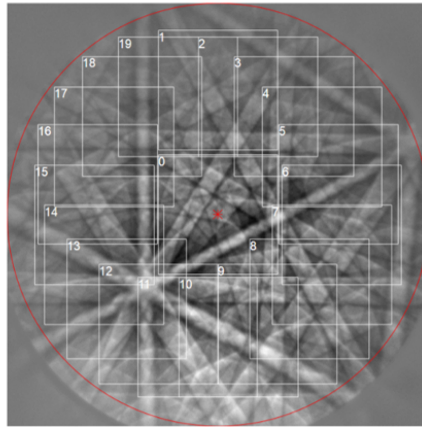

Figure 2.11: Allocation of the ROIs

calculate a relative distortion matrix [28]. From these matrices the stress and strain of the material in each point are calculated [26].

2.3 Tungsten Carbide

2.3.1 Sintering

Tungsten-carbide is a material made of tungsten (W) and carbon (C). Together with cobalt it is possible to produce parts with a Vickers number of around $HV = 2030$ [29] and a compressive strength of about $4 - 9\ GPa$ [30]. The Vickers number gives a value for a material's hardness, and is determined by indentation with a pyramid-shaped diamond. In soft material, the diamond leaves a bigger indentation. For stainless steel HV is usually smaller than 500. The compressive strength is a material's ability to withstand being pushed together. WC-Co work pieces are mostly used as cutting or drilling tools presented in figure 2.12a. However, they also are used as ammunition, surgical instruments and other applications. WC is a powder of grainsize $0.5 - 7\ \mu m$. To produce a work piece, it is necessary to sinter WC together with Co. Therefore WC and Co powder is mixed up. The Co serves as a binder phase and

typically $5 - 20$ % of the weight is Co. Under high temperature and pressure the powder is sintered and loses several percent of the volume. A work piece before and after the sintering process is displayed in figure 2.12b. After sintering the work piece is ground into its final shape. In this present work, coarse grain samples ($2.5 - 6\ \mu m$) with a high amount of Co were investigated. The Co amount is at about 20 wt%.

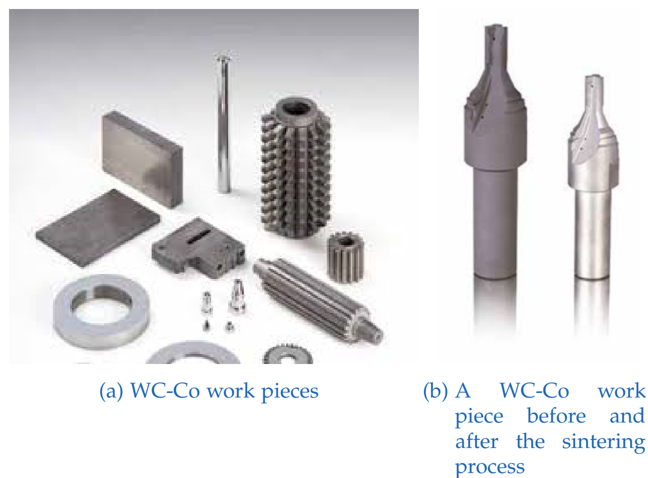

(a) WC-Co work pieces

(b) A WC-Co work piece before and after the sintering process

Figure 2.12: Image of cemented carbide work pieces [31]

2.3.2 Magnetic Saturation

The magnetic saturation is measured by the strength of the magnetic field of the cobalt binder phase. The strength of the magnetic field is dependent on the amount of W and C dissolved in the cobalt, so the C and W amount in the binder is measured indirectly via the magnetic saturation. The sintering process leads to dissolving W and C into the Co binder phase. Since Co is the only compound with magnetic properties, pure Co has the highest magnetic saturation. The more W is solved in the Co phase, the less magnetic saturation can be measured in the material. Also the C amount in the WC is indirectly proportional to the magnetic saturation of the Co due to worse solving properties of WC with higher C concentration [32]. The C concentration also has influence on hardness and strength.

3 Experimental Procedure

In this chapter the experimental procedure is introduced. The examination process is visualised in figure 3.1. It consists of four main steps, each sample was going through several of these steps. Depending on the sample, the starting step varied. All samples were undergoing the steps from their starting point to "Step four: Evaluation and calculations". The starting point of the sample is indicated with green arrows.

"Step one: Surface treatment" is the grinding process explained in detail in section 3.1.1. "Ground" samples started with this procedure.

To analyse the influence of surface treatment on stress levels, samples with ground and untreated surface were compared. The samples with untreated surfaces did not undergo surface treatment and started at "Step two: Measurement preparation". This step (section 3.2) was necessary to polish the cross sections to make EBSD studies possible, which are very sensitive to surface defects or roughness.

Due to a suitable surface the Si wafer did not need further surface treatment and was directly examined in "Step three: Measurements" (section 3.3 and 3.4). The Si wafer started at point three and was examined for calibration purposes and to evaluate the reliability of the values calculated by the CC4 software.

All measurement results were analysed with OIM Systems [10], CC4 and Matlab as mentioned in "Step four: Evaluation and calculations". Step four is explained in section 3.5.

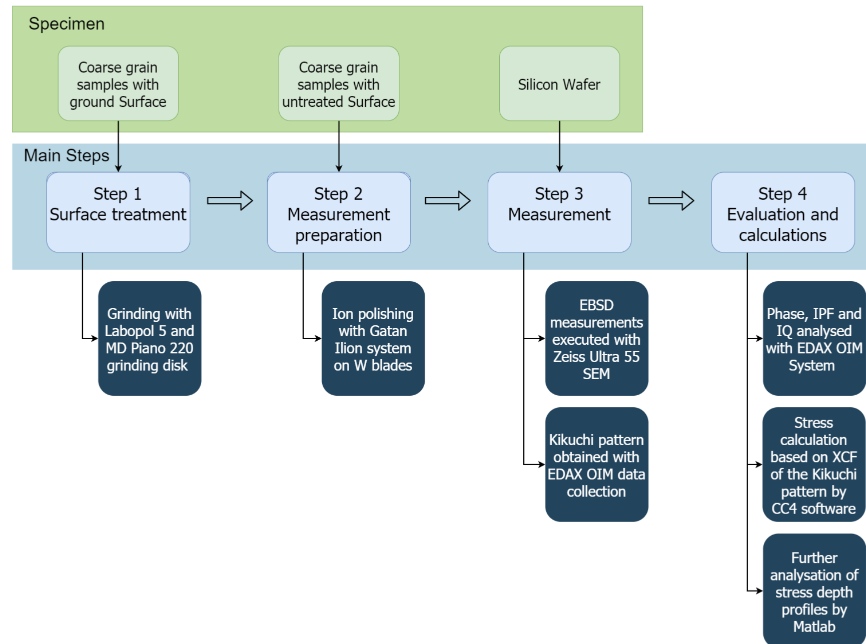

Figure 3.1: Diagram of the experimental process used in this thesis

3.1 Surface Treatment

3.1.1 Grinding Process

Generally, manufacturers process sintered WC-Co work pieces by grinding them to their final shape as part of their manufacturing process. This leads to the interest in the influence of surface treatment and especially grinding processes on the stress level, since stress has a great influence on the resistivity of a WC-Co work piece.

The sintered WC-Co was examined with and without prior grinding done by the author in order to get an impression of the influence of surface treatment on the stress levels on the surface. The raw, only sintered samples were prepared for the SEM examination by means of slope cutter ion polishing preparation without further mechanical processing and serve as reference. The samples ”with ground surface” did undergo a further surface treatment. This surface treatment was a

grinding process executed with the Struers LaboPol 5 polisher, which allows to use exact the same grinding parameters for each sample. The grinding was performed with 200 revolutions per minute, on the 3rd pressure ring, with the MD piano 220 grinding disk for 4 minutes. DP-lubricant Yellow was taken as lubricant.

3.2 Sample Preparation

In this section, the treatment of the samples is explained. Ideally, a sample has a plain surface big enough for EBSD measurements. In this thesis the examined areas of the WC-Co samples expand over $20x20$ μm^2 and $12x12$ μm^2. Since the influence of grinding and polishing on stress occurring at the surface of a cemented carbide is investigated in this present work, it was necessary to avoid inducing extra stress into the surface by grinding and polishing. To provide a sample preparation without severe surface damage, the samples were processed with a Gatan Ilion™ion polisher.

The ion mill sputters parts of the sample to expose a cross section which can be examined. With this method, no further stress is embedded into the sample. The impact of the argon (Ar)-ions accelerated onto the sample is limited to several nm. The BSEs arrive from a depth of several tens of nm so the damage has little impact on the obtained Kikuchi patterns. Radi et al. [33] examined the preparation method for EBSD measurement in terms of the beam incident angle and approve this preparation method with the suggestion that damage- and oxygen-free surfaces are crucial for good EBSD results.

In addition the sample should have a good conductivity in order to conduct charges due to the electrons induced into the sample by the SEM.

3.2.1 Ion Polishing

The samples were glued on a blade made of W or titanium (Ti) with conductive silver so that the sample protrudes approximately 110 μm over the blade. The blade serves to shield the sample from the ion beam, so that the ions thin off part of the protruding sample as shown in figure 3.2. A smooth surface directly at the edge is crucial, since the surface cross sections are located directly at the sample edge.

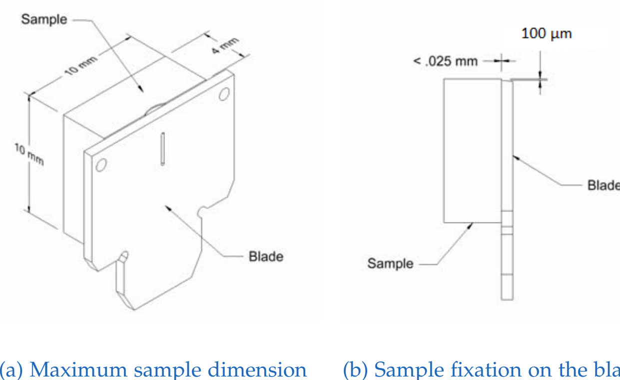

(a) Maximum sample dimension (b) Sample fixation on the blade

Figure 3.2: Sketch of a sample glued to a blade from the Ilion™"Precision Cross-Section System Owner's Manual and User's Guide".

The impact of ion bombardment on the blade is visible in figure 3.3a. Other glue materials like copper tape and super glue were tested, but discarded due to bad conductivity. The polishing process was done at 6 keV ion energy for 2 to 6 hours. The polishing time varied in order to provide a surface well suited for EBSD measurements, but mostly around 4 hours. The direction of the Ar - ions during the polishing process is sketched in figure 3.4. An SE image of a sample with Ar - ion polished area is displayed in figure 3.3b.

A problem, not yet overcome, are curtaining effects. Caused by the mechanisms of the ion milling process, the surface has uneven grooves. This curtaining effect leads to areas out of focus in the grooves and therefore to measurements and areas with bad image quality (IQ). The bad image quality leads to unrealistic high stress values in some areas. The curtaining effects can be induced by the grains of the blade, the glue

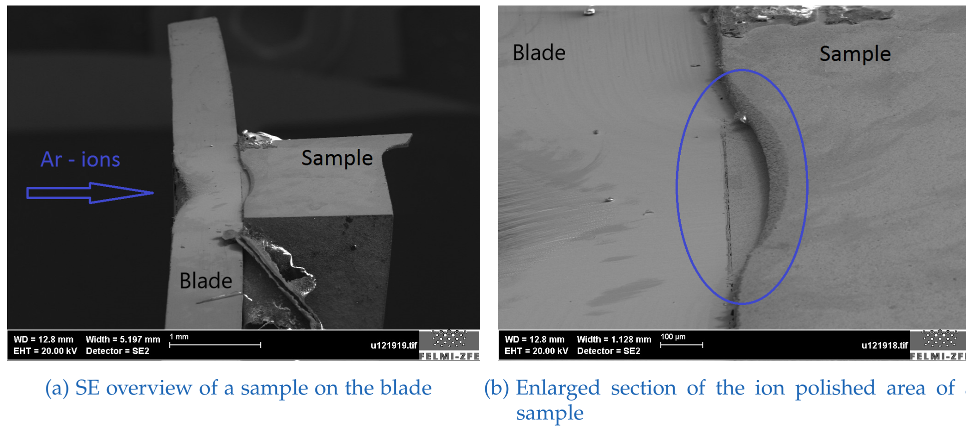

(a) SE overview of a sample on the blade

(b) Enlarged section of the ion polished area of a sample

Figure 3.3: SE images of a WC-Co sample with low magnetic saturation and ground surface

and the sample itself. In coarse-grained samples the curtaining effect is stronger than in fine grain samples due to non-uniformly distributed areas of high hardness (WC) and lower hardness (Co). Considerations on how the curtaining effect affects the results are given in section 5.1.2.

3.3 Scanning Electron Microscope

SEM Setup

The samples were tilted to 70° and examined with a Zeiss Ultra 55 SEM. All measurements were obtained at a high voltage of 20 kV. A working distance, the distance between the pole pieces of the SEM and the sample surface, of 12 to 15 mm turned out to be suitable, and was used during the measurements. In order to obtain a high electron intensity, an aperture of 120 μm was chosen, and "high current" was used which results in a beam current of 12 nA. The area was focused via SE, and then EBSD measurements were executed. Exemplary SE images of a WC-Co sample with low magnetic saturation are displayed in figure 3.3 for an impression of the sample. The high electron intensity was necessary to obtain enough signal for the diffraction pattern on the phosphor screen. To enable a viable impression of the influence of the magnetic saturation and of surface treatment on the sample, cross section measurements were executed far enough in the bulk of the sample so there was no influence of surface phenomena. In the following, these areas are referred to as bulk cross sections. Surface treatment comparisons were done with cross section measurements directly at the ground or untreated surface. These areas are the surface cross sections. Figure 3.4 sketches the position of the bulk cross section and the surface cross section. Figure 3.5 shows a 3D model of the sample.

3.4 OIM Data Collection

3.4.1 OIM Data Collection Settings

For the recording of the Kikuchi patterns the EDAX OIM Data Collection Software [10] was used. The recording of the Kikuchi patterns was performed with an exposure time of about 60 ms. The Kikuchi patterns were obtain by integrative averaging of 2 recorded Kikuchi patterns from the same measurement point. Depending on the measurement either $1x1$

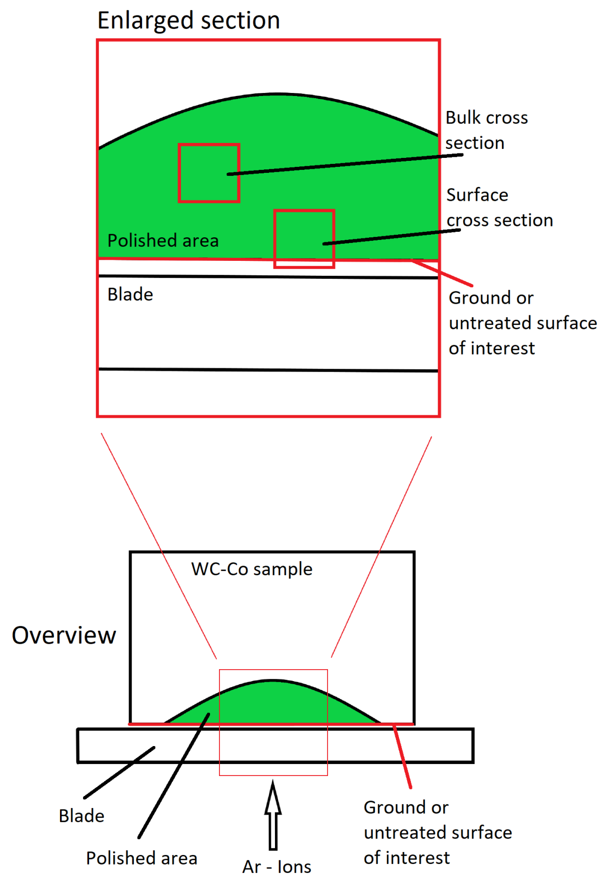

Figure 3.4: Sketch of the investigated cross sections

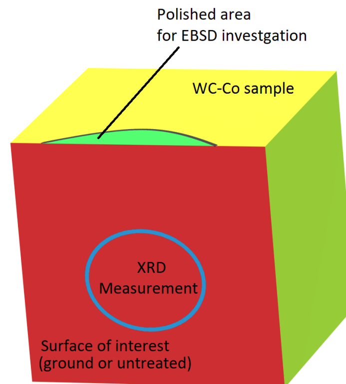

Figure 3.5: Model of the investigated surfaces of the sample. The sample is mounted onto the blade with the red indicated surface of interest for ion polishing and further EBSD investigations. For XRD analysis the surface does not need further preparation, so the XRD measurement is executed directly at the surface of interest.

or $2x2$ *binning* was used for the measurements. The stepsize of the PE beam was chosen between 50 and 200 *nm*. The background correction was processed with 40 images. The background correction is necessary due to the fact that raw Kikuchi patterns are often noisy and of low contrast. The background correction calculates the average of a given number of pictures and subtracts these from each pattern. The gain, which represents the photo sensitivity of the CCD, was set to have a brightness of about 0.7.

3.5 CC4 Software

In the following, the calibration and settings of the CC4 software is presented. Figure 3.6 gives an overview of the course of calculations and shows the multitude of results obtainable with the software. This thesis is based on the analysis of the shifts and stress results given by the CC4 software.

3.5.1 Elastic Coefficients

As mentioned before, the elastic coefficients are important for further calculations in the CC4 software. The elastic coefficients of the software for different phases and crystal structures are pre-installed. These pre-installed values were taken for Si in sc, WC in hexagonal closed pack (hcp) and Co in hcp and face centered cubic (fcc) for all calculations.

3.5.2 CC4 Calibration of Effective Pixel Size

The CC4 software calculates a relative residual stress value by comparing the Kikuchi patterns obtained by EBSD with XCFs. This means, the difference between two Kikuchi pattern result in a relative value defining the stress difference between these two Kikuchi patterns. Alterations or shifts of Kikuchi patterns can be caused by different types of crystal defects or residual stress as explained in section 2.1.1. One additional origin for the alterations of the Kikuchi patterns is the scanning move of the electron beam. This scanning move of the electron beam induces a linear shift of the Kikuchi patterns. Therefore two effects are overlaying causing pattern shifts in the Kikuchi patterns, the linear pattern shift of the beam mechanics and the non linear pattern shifts, depending on the stress within the crystal.

Since the CC4 software is not able to recognize the origin of the pattern shift, and only the pattern shifts due to the stress should be examined, the beam shift correction is crucial. The beam shift could be eliminated by moving the stage instead of the electron beam. This is a time consuming process, which is why the shift generated by the scanning of the beam is eliminated by calibrating and using the beam shift correction. This so called beam shift correction is the tool of the CC4 software eliminating the linear shift of the Kikuchi patterns caused by the movement of the scanning beam. The principle of the shifted PE beam is shown in figure 3.7a. At each new scanning point, a full new pattern is produced on the screen. The linear scanning move of the PE beam induces a linear shift of the Kikuchi pattern on the phosphor screen. The CC4 software eliminates this linear shift prior to further calculations by applying the beam shift

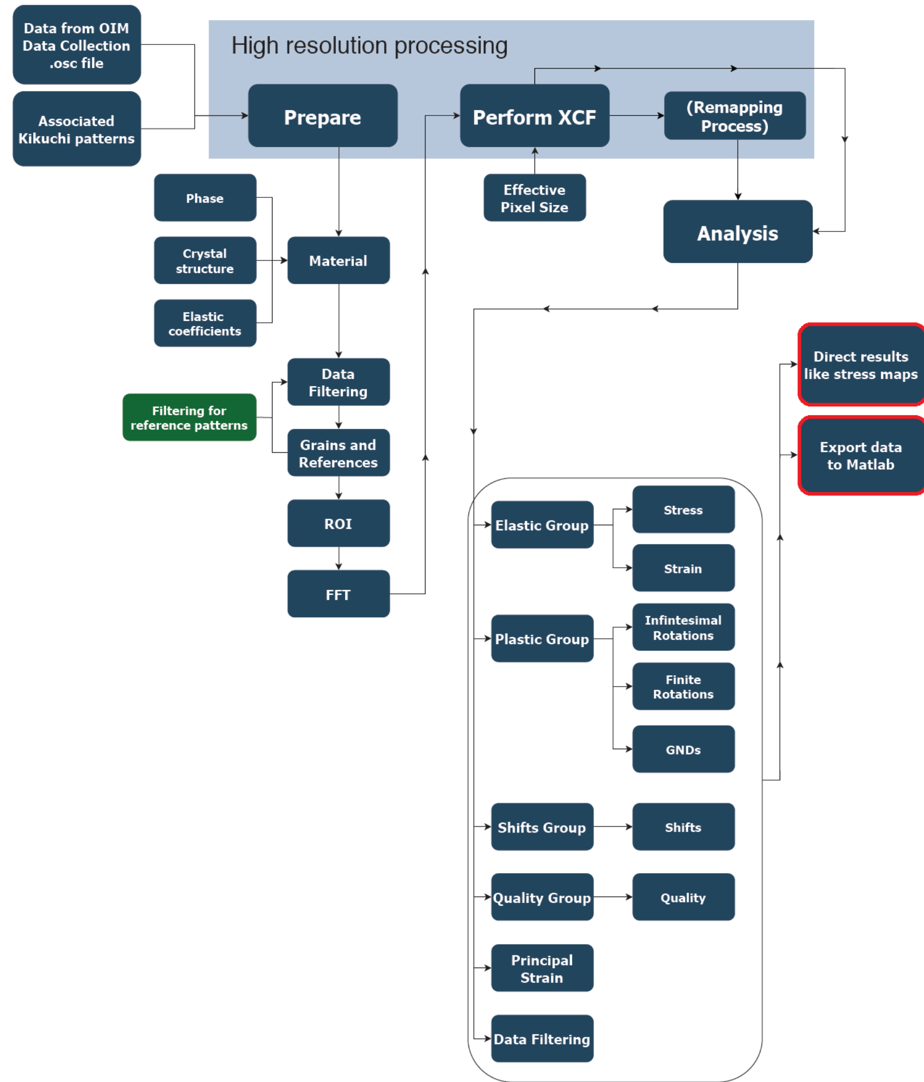

Figure 3.6: Diagram of the CC4 software. Within this present work stress and shifts were evaluated.

correction. The beam shift correction is based on the calculation of the effective pixel size. The effective pixel size is the real side length of the area on the phosphor screen recorded by one pixel of the CCD. The CCD camera is not sketched in figure 3.7a, figure 2.4a shows the full experimental setup. This length is calculated by analysing the shift of the pattern center in x-direction. This is based on the fact, that the stepsize of the PE beam is known.

The pattern center on the screen is a special point within the Kikuchi pattern and directly connected to the scanning move of the electron beam. The intersection of the phosphor screen and the line orthogonal to it, through the point where the incident electron beam hits the sample, is defined as the pattern center. In figure 3.7a the pattern center is indicated by the abbreviation 'pc'. This is due to the fact that the Kikuchi pattern is not a reflection of the incident beam but is assembled by electrons scattered back by the crystal lattice of the sample. A sketch of the position of the pattern center is shown in figure 3.7b. Caused by the geometrics of the pattern centre, it is the point which is not moving when the phosphor screen is moved in or out. In the case of a stress free sample, the construction of the pattern centre via an orthogonal line through the incident point of the electrons causes the position of the pattern center to move exactly in the same manner as the incident point of the electrons on the sample. This movement of the pattern centre due to the scanning move of the beam is sketched in figure 3.7a. The sketch shows the scanning points of the electron beam on the sample. For every point a Kikuchi pattern is recorded. The Kikuchi patterns are shifted on the phosphor screen depending on the position of the scanning point relative to the reference pattern. Together with the Kikuchi patterns, the pattern center is also shifted.

Based on this movement of the shifts of the pattern center the effective pixel size is calculated. Therefore a sample without stress is necessary to obtain only the linear pattern shift of the scanning of the beam. Since the pattern shifts are dependent on the distance from the reference pattern, just one direction has to be calculated to determine the effective pixel size. Therefore the pattern shifts occurring in a line scan are analysed. The pattern for each measurement point can be shifted in x and y direction as sketched in figure 3.8. The two squares indicate two full Kikuchi patterns,

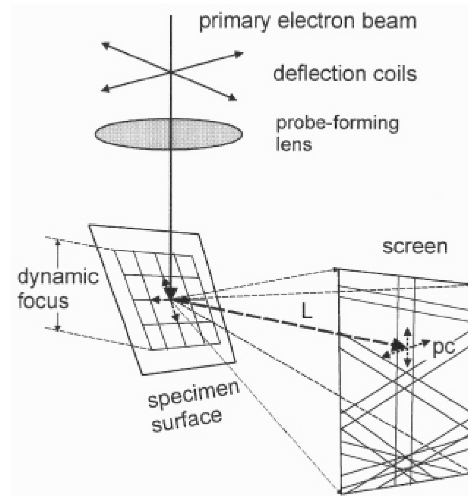

(a) Sketch of the mechanics of the electron beam. The image is taken from Schwarzer [34].

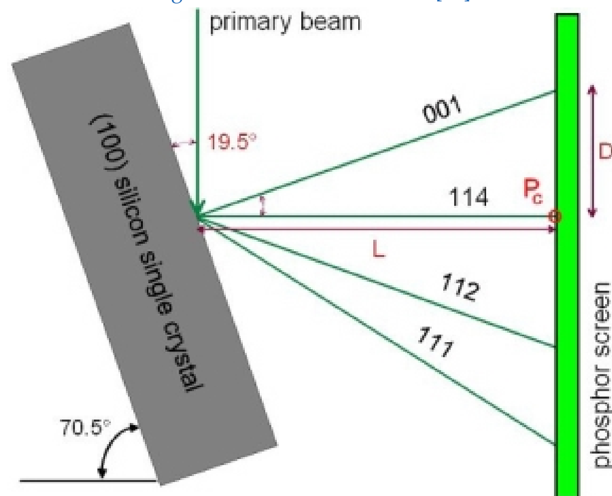

(b) Sketch of the position of the pattern centre. In this present work the sample is tilted about 70°. The incident angle of the PE beam is about 20°. The sketch is taken from "Basics of EBSD and BKD" [35].

Figure 3.7: Sketches of the beam mechanics and the position of the pattern centre. The pattern centre is indicated in both images with pc. The pattern centre is obtained by laying a straight line through the incident point of the electron beam on the sample, normal to the phosphor screen.

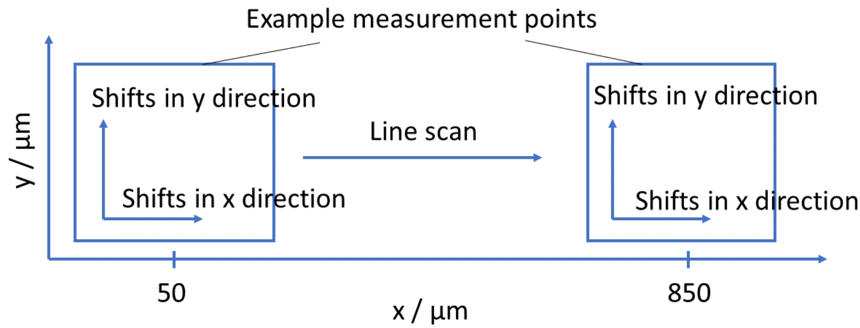

Figure 3.8: Sketch of the shifts in x- and y-direction of the measurement points of a line scan. The unit of the shifts are pixels, calculated by the CC4 software. In the measurements covering an area, there is also more than just one line in y-direction. In this case of a Si wafer, the crystal has an expansion of far more than 1 mm so the Kikuchi pattern stays very similar over the whole length. Only a small pattern shift originating in the shift of the PE beam should be observable.

referring to different positions of the PE beam. The beam shift correction eliminates the linear distortions of the patterns, caused by shifts in x-direction and shifts in y-direction, from further calculations. This is based on the assumption, that the pattern shifts due to the beam movement are isotropic on the observed surface and only defined by the distance to the reference pattern. When the sample is placed in a manner, that the scanned line from the line scan is exactly parallel to the phosphor screen (as is the case in figure 3.7a), the obtained Kikuchi patterns have zero pattern shifts in y direction and the Kikuchi patterns should only be shifted in the x direction. A crystal without stress whatsoever would just show pattern shifts originating from the scanning of the beam, so these shifts should show a linear behaviour. To calculate the effective pixel size, the length of the line scan on the sample is divided by the obtained shifts in x direction as in equation 3.1.

$$\text{Effective Pixel Size}\left[\frac{\mu m}{Pixel}\right] = \frac{\text{Scanned Length of the Linescan}\ [\mu m]}{\text{Shifts in X-Direction}\ [Pixel]} \tag{3.1}$$

For the calculation of the effective pixel size it is necessary to analyse the shifts of a line scan. In order to obtain just the linear shifts originating in the movement of the scanning beam, the investigated sample should be stress free. The pattern center is one certain point of the Kikuchi pattern. This means the pattern center is shifted together with the Kikuchi pattern. Therefore the beam shift correction can be calibrated in the CC4 software by analysing the shift of the pattern centre. This is done by placing one ROI directly onto the pattern centre. The effective pixel size is calculated for the shift of this certain ROI. This shift is caused by the scanning move of the PE beam and can be recognised by the position of the pattern center or the Kikuchi pattern on the phosphor screen. Since the analysed sample is considered to be stress free, it can be assumed that two identical Kikuchi pattern are just shifted by the shift of the PE beam. Using the XCF, the CC4 software can compare these two shifted Kikuchi patterns and calculate the shift between those patterns. The calculations give the shift between the two patterns in pixels. The CC4 software represents the shifts in pixels for each ROI of the recorded Kikuchi patterns. The dimensions and with them the length of the line scan can be taken from the measurement properties. By defining a reference pattern, an arbitrary zero point is chosen. The XCF calculates the shifts of the Kikuchi patterns with respect to this arbitrary zero point. The PE beam shift is known from the stepsize. The Kikuchi pattern (x) positions on the sample can be calculated with the stepsize. These two values, the nearly linear pattern shifts in x direction and the (x) position of the measurement on the sample can be drawn in a nearly linear graph together, showing the pattern shift dependent on the (x) position of the PE beam on the sample. This is done for the later carried out calibration with the blue line in figure 3.9a. The idea is now, to eliminate this linear shift by telling the software the connection between the movement of the beam on the sample and the movement of the Kikuchi pattern on the phosphor screen. This connection is the effective pixel size. Since the measurements ideally are carried out on a sample free of stress, the effective pixel size can be calculated according to equation 3.1, by dividing the length of the line scan by the total shift (difference between the shift of the first measurement point and the last measurement point). For the calculation the values needed in eq. 3.1 are results of the software. With these, one can calculate the effective pixel size. The special interest in the x direction is due to the

isotropic relation on the measured surface between the PE beam shift and the Kikuchi patterns. This shift is only dependend on the distance on the sample of the evaluated measurement point and the scanning point of the reference pattern. The beam shift correction eliminates the pattern shifts in x and in y direction from further calculations. The graph of the corrected pattern shifts for the later carried out calibration are presented with the red line in figure 3.9a.

Since the effective pixel size is the real side length of the area on the phosphor screen recorded by one pixel, binning also has an influence on the beam shift correction. With $2x2$ binning one "virtual" pixel has double the side length of a pixel with $1x1$ binning. Binning is a technique in which the signal of several pixel is summed. Advantages in doing so are more intense signal for the picture of the Kikuchi patterns. Therefore shorter exposure times are necessary and a better contrast is reached due to a lower gain level. The disadvantage is the loss of information due to less pixels per pattern (in the case of $2x2$ binning: $512x512$ *pixels* instead of $1024x1024$ *pixels*).

The calibration of the effective pixel size was executed on a Si wafer, assuming low residual stress levels within a Si single crystal and therefore low pattern shifts caused by residual stress. The obtained pattern shifts in x-direction are 22.48 *pixels* on a length of 900 μm. With equation 3.1 these values lead to an effective pixel size of 40.04 $\mu m/pixel$ (equation 3.2). The values are visible in figure 3.9. Many of the measurements were executed with $2x2$ binning. $2x2$ binning leads to an effective pixel size of 80.08 $\mu m/pixel$ for one bin.

$$\text{Effective Pixel Size} = \frac{900\ \mu m}{22.48\ Pixel} = 40.04 \frac{\mu m}{Pixel} \tag{3.2}$$

Figure 3.9 shows the pixel shifts of the Kikuchi pattern in x-direction (figure 3.9a) and in y-direction (figure 3.9b) for a line scan. The shifts were calculated with and without beam shift correction, calibrated with the effective pixel size. With use of the beam shift correction, the shift over the full 900 μm is 0.1 *pixel* with a variation range of 0.41 *pixels*. The shifts

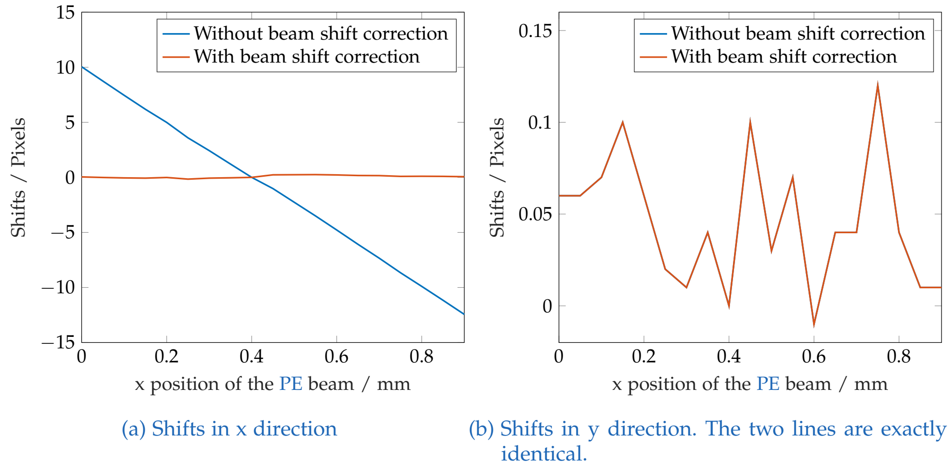

(a) Shifts in x direction

(b) Shifts in y direction. The two lines are exactly identical.

Figure 3.9: Representation of the pixel shifts identified on the phosphor screen by XCF versus the shift of the PE beam. The graphs show the shifts with and without beam shift correction.

in y-direction are not changed by the beam shift correction. This is due to the fact that the line scan only has one position for y. In measurements covering areas multiple positions for y are measured resulting in shifts in y direction originating from the beam shift occur. These shifts are also considered and corrected by the beam shift correction.

The influence of the beam shift calibration on the obtained residual stress values is demonstrated in figure 3.10. A calculation without beam shift correction is shown in figure 3.10a. The movement of the Kikuchi pattern and therefore the calculated values of the residual stress are directly proportional to the distance between the observed measurement point and the chosen reference pattern. This lets the stress values raise circular around the reference pattern. To eliminate this pattern movement, the effective pixels size is calculated, and the beam shift correction is calibrated. With elimination of this pattern movement the stress map shows the expected low stress values as demonstrated in figure 3.10b.

An estimation of the quality of the beam shift calibration is done for an area of $200x200$ μm^2 of the Si wafer. The corrected and uncorrected σ_{11} and σ_{VM} stress profiles are visible in figure 3.11. The Si wafer is assumed to be free of stress, so these σ_{11} stress profile (figure 3.11a) ideally should

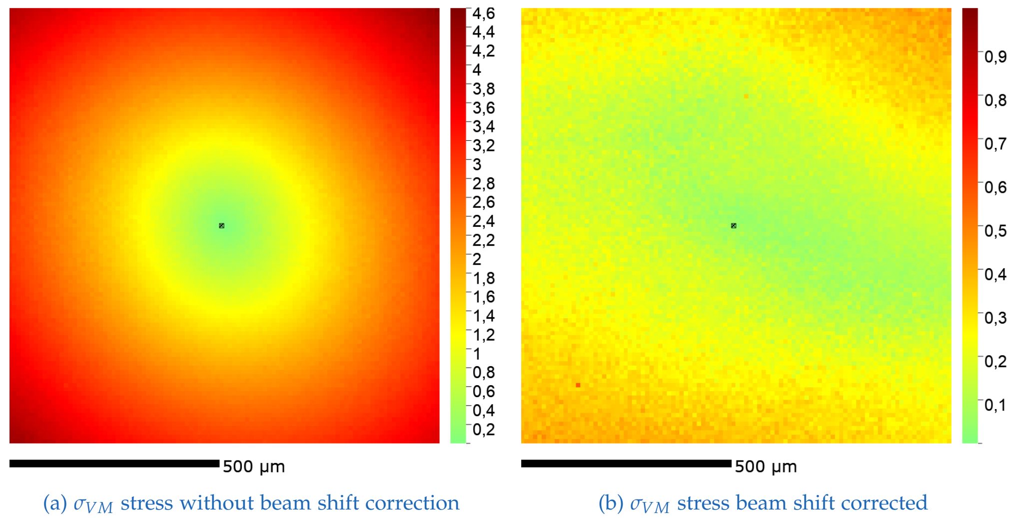

(a) σ_{VM} stress without beam shift correction

(b) σ_{VM} stress beam shift corrected

Figure 3.10: σ_{VM} stress maps for a silicon wafer calculated with and without beam shift correction. The black squares in the middle of the stress maps indicate the position of the reference pattern.

not show any stress. However after the correction the σ_{11} stress profile shows stress values between -0.005 and 0.025 GPa. The higher values in the σ_{VM} stress profile (figure 3.11b) after the correction is due to the calculation of the von Mises stress (equation 2.4). The 30 MPa difference in the σ_{11} stress profile seems to be no significant error source considering results of 200 MPa and more.

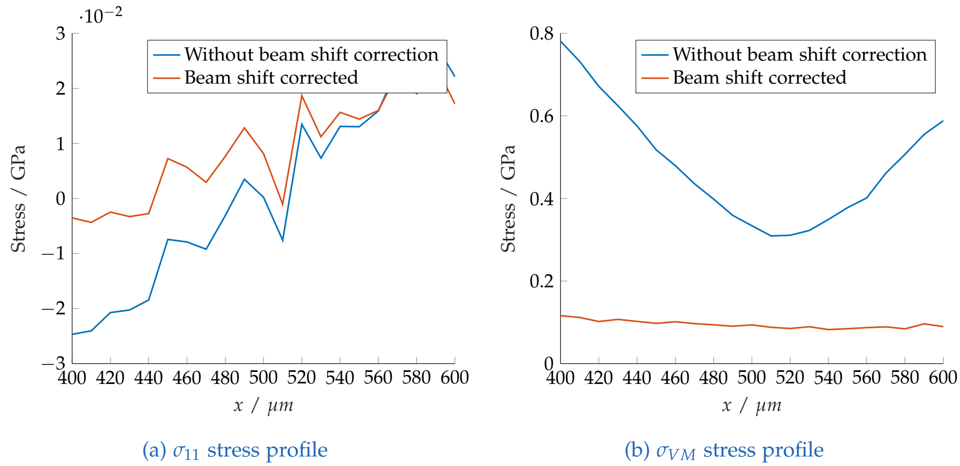

(a) σ_{11} stress profile

(b) σ_{VM} stress profile

Figure 3.11: Stress profile of a 200x200 μm^2 area of an Si wafer with and without beam shift calibration. The variation from linearity is assumed to originate from residual stress within the Si wafer.

3.5.3 Data Filtering for Reference Pattern

The CC4 software searches for the pattern with the lowest KAM and sets it automatically as the reference Kikuchi pattern [26]. The KAM is the misorientation of one measurement point to its neighbours [36]. The KAM gives a first idea of the distortion of the examined crystal. Ideally, the reference pattern has to be free of strain. Every reference pattern covers a certain rotation. This rotation can be defined in the CC4 software. When this maximum rotation for one reference pattern is exceeded within one grain, a second reference pattern is necessary. Within some large grains and grains with very high lattice rotation angles, multiple reference patterns are used. Since stress is calculated as a relative value referring to the reference pattern, a bad reference pattern results in wrong stress values for the grain. In cases where multiple reference patterns are necessary, these patterns are often placed in highly rotated areas, since these are the areas not covered by other reference patterns. The software takes one of the reference points as zero, and calculates the relative stress between the reference points. When the reference pattern chosen as zero lies in a highly rotated or stressed area, the grain is calculated to very high stress and strain values over the whole are as

demonstrated in figure 3.12a. Especially the grains directly on the surface show uniformly high stress values.

In order to avoid grains which are high strained and stressed uniformly over the whole area, it turned out to be useful to exclude some of the bad patterns from being chosen as reference patterns. This is necessary due to the relative nature of the obtained stress values. A grain with just one point with a low stress level is often a sign for a bad chosen reference pattern. So before defining the reference patterns, all pixels with an IQ lower than 30000 were excluded, and then added afterwards. The IQ is a value associated to every pixel by the OIM data collection and gives a value for the quality of the Kikuchi pattern. A good pattern has values of about 50000 - 60000. The limit of 30000 showed to be suitable for this present work. This procedure corrects the calculated stress values because a realistic zero pattern is chosen, but excludes some of the pixels from the calculation, when they cannot be calculated with the given reference patterns. The evaluations in figure 3.12b were executed using a quality filter for the reference patterns. The grains directly at the surface show a progressing behaviour over the whole grain. Due to the relative approach of the evaluation the surface grains in this map correspond to the expected behaviour of a progression of stress values within the grain, as it seems rather unlikely for grains to be highly stressed with one pixel as exception. There are regions which are not covered by the allowed rotation conventions for the reference patterns indicated white in the stress map. These white pixels can either be too high for the color scale or out of reach for the chosen reference patterns.

3.5.4 Fast Fourier Transformation

A fast Fourier transformation is used to filter high frequency (HF) information and low frequency (LF) information of images, before further image analysis and the calculation of the XCF is done. Sharp changes within patterns are represented by HF components, whereas LF components of the pattern are containing information concerning long range contrast changes [26]. The high frequency cut-off and low frequency cut-off of the fast Fourier transformation (FFT) were set up analysing the

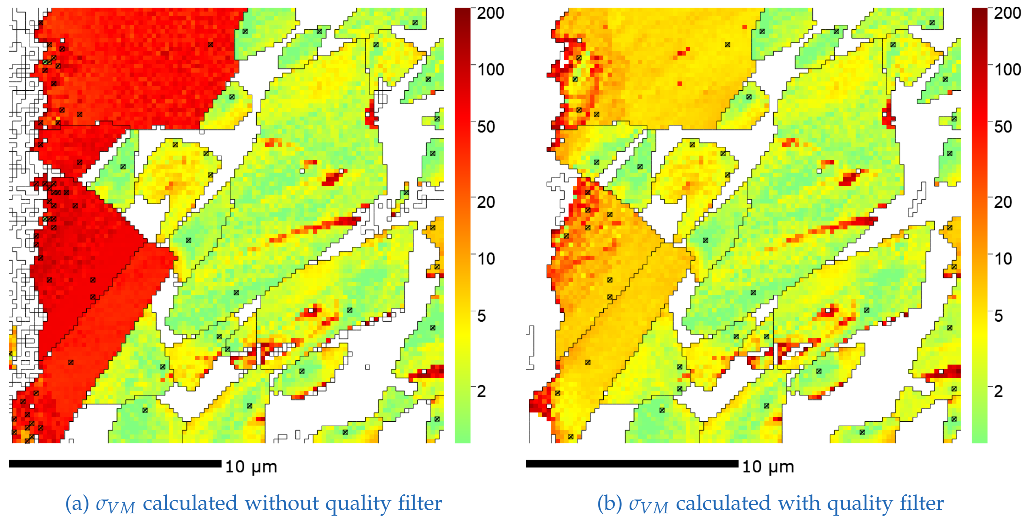

(a) σ_{VM} calculated without quality filter

(b) σ_{VM} calculated with quality filter

Figure 3.12: Comparison of two different settings for defining the reference patterns for the evaluation of the WC phase of a surface cross section of a sample with high magnetic saturation and ground surface.

shifts of a Si wafer line scan. Ideally the Si wafer should be free of stress, therefore the shifts are expected to show linear behaviour. To evaluate the optimal settings for the high frequency cut-off and low frequency cut-off, a 'high' setting and a 'low' setting was chosen for the HF and LF cut-offs. The HF cut-off settings where chosen to 27 for low and 70 for high and the LF cut-off values were chosen to 2 and 6. The shifts where evaluated for the 4 possible combinations of this settings as listed in table 3.1. The optimal value with the least variance to linearity, was found to be at 2 for the LF cut-off and 27 for the HF cut-off. Therefore these settings for the FFT are expected to lead to the best results. The calculated variances for different FFT parameters are presented in table 3.1. However, these values result in very high stress values demonstrated in the stress map in figure 3.13b. One possible problem for these seemingly 'sharp' settings could be the surface preparation. The shape of the high stressed areas is similar to the uneven grooves in the surface, which are due to the Ilion™ion polisher and discussed in section 5.1.2. A perfect surface would probably bring good results with a sharp setting like 2 for LF cutoff and 27 for HF cutoff. Further calculations suggested the use of the preset values of the CC4 software (LF cutoff: 6, HF cutoff: 27),

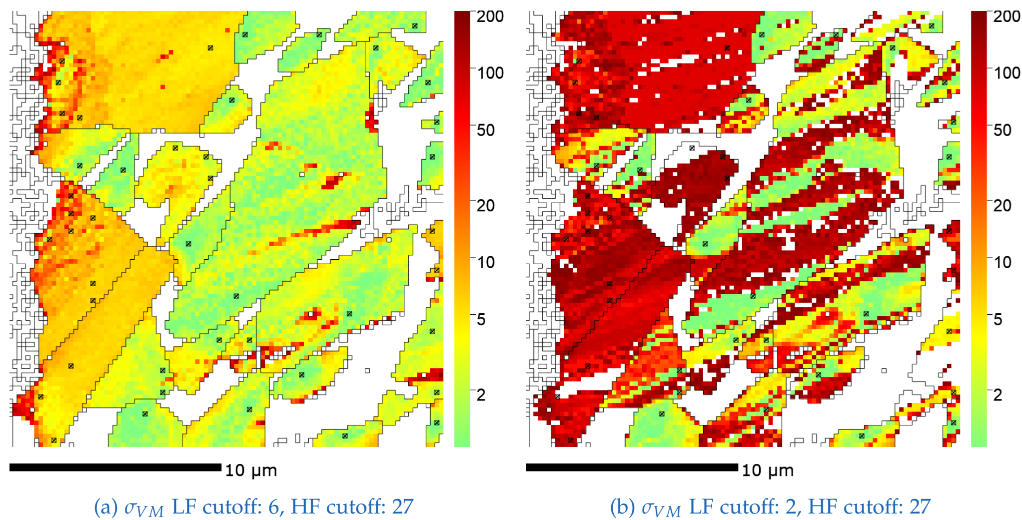

(a) σ_{VM} LF cutoff: 6, HF cutoff: 27

(b) σ_{VM} LF cutoff: 2, HF cutoff: 27

Figure 3.13: Comparison of the two different FFT settings for the evaluation of the WC phase of a surface cross section of a sample with high magnetic saturation and ground surface.

since the fitted values resulted in high stress values several factors above the expected maximum of about 10 GPa. Figure 3.13 demonstrates the significant difference between the values of the LF and HF cutoff. Taking the preset values (figure 3.13a) seemed to smoothen the surface and to decrease the influence of the grooves.

The FFT filter was calibrated with help of the sample shift as presented above. The calculated values corresponding best to the expected linear shift (due to very low residual stress levels expected within the Si wafer) were 2 for the LF cutoff and 27 for the HF cutoff. Stress calculation using these HF and LF cutoff values for the FFT is compared to the preset values of the CC4 software which are 6 for LF cutoff and 27 for HF cutoff. Figure 3.14 shows the mean stress profile for σ_{11} (figure 3.14a) and for σ_{VM} (figure 3.14b) within the WC phase of a WC-Co sample. Both diagrams show average stress values for single lines far above 10 $GPa(\sigma_{11})$ and 50 GPa (σ_{VM}). A filter for the calculated stress values was introduced due to considerations presented in section 3.5.5. The filter eliminates stress values above 30 GPa. The filtered mean stress values for the XRD comparison region are similar with 6.44 GPa (LF: 6, HF: 27) and 6.19 GPa

Table 3.1: Errors of the FFT parameterfit

LF cutoff Low Frequency Cutoff
HF cutoff High Frequency Cutoff
variance to linearity

LF cutoff	HF cutoff	variance
2	27	0,14
2	70	0,44
6	27	0,26
6	70	0,78

(LF: 2, HF: 27). The difference lies in the percentage of values eliminated by the filter. LF: 6 and HF: 27 had an elimination percentage of 2.4% whereas for LF: 2 and HF: 27 the filter eliminated 75% of the stress values before calculating the mean stress value. The graphs in figure 3.14 show stress level within the WC phase of a WC-Co sample and are displayed without the 30 GPa filter. However, using the values suggested by the calibration of the pattern shifts, leads to values far above the upper filter limit of 30 GPa for σ_{VM}. Zhu et al. [20] simulated a maximum residual stress value of under 10 GPa for the von Mises stress of WC grains. More realistic and expected values are obtained by using the default values from the CC4 software for the FFT settings.

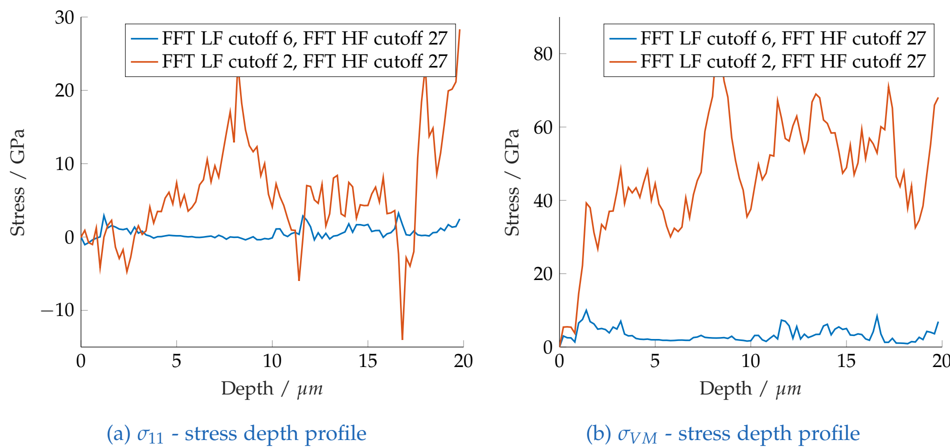

(a) σ_{11} - stress depth profile

(b) σ_{VM} - stress depth profile

Figure 3.14: Stress depth profile within the WC phase of a WC-Co sample of a surface cross section of a sample with high magnetic saturation and ground surface.

3.5.5 Matlab Evaluation

Stress Depth Profile

A stress depth profile for the surface cross sections and for the bulk cross section was calculated for most of the samples using Matlab. The Matlab calculations were used to reach a better comparability of the values gained by the CC4 software and aim to get better quantitative results. The stress profile averages all values for one x position (i.e. for a certain depth). The mean values calculated for all x positions give the mean stress profile. A sketch of the calculation of the mean stress profile is provided in figure 3.15. The assumption concerning the influence of surface treatment on residual stress levels was that the influence is limited to one or maximal a few grain sizes into the sample. Therefore the mean stress profile diagram is used to examine the depth of the influence of the grinding process. It starts at the surface (the first point which is addressed to a grain), which is the zero point, and shows the development of stress with increasing depth. The result is a line vector with a mean stress value for every depth, starting at the surface.

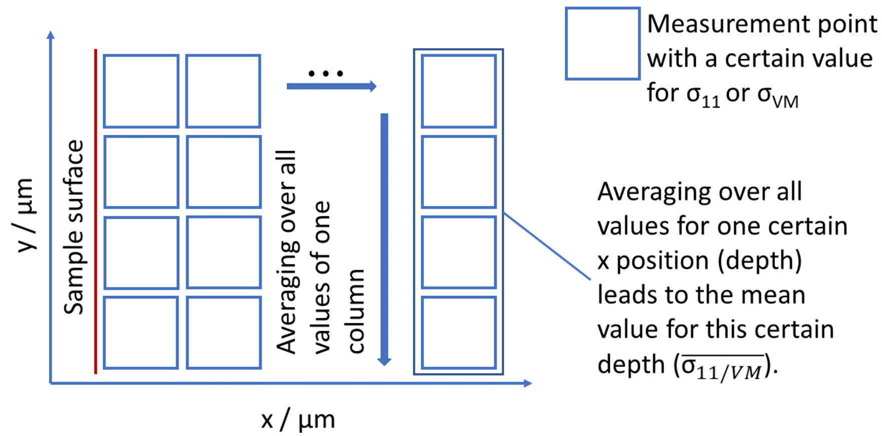

Figure 3.15: Sketch of the calculation of the mean stress profile

XRD Comparison Region

The depth reached by an XRD measurement is limited to about 3 μm into the sample. The Matlab script calculates the mean stress value for the first 3 μm into the sample, starting from the surface. At the bulk cross sections, the mean stress value for the whole measured area is calculated, averaging the whole stress map.

Filter

Phenomena like overlaying Kikuchi patterns lead to unrealistic high stress values as a consequence of the type of evaluation. In order to solve this issue a filter was used to eliminate these unrealistic high values. Since the evaluated values are mean values the values were defined as outliers above about five times the calculated mean value. Since the composition of the examined material changes just marginally, the same upper limit of values was chosen for all calculations, based on the maximum means stress value calculated, which is 6.44 GPa for WC in the ground sample with high magnetic saturation. The filter was

rounded to 30 GPa. The limit is based on the considerations introduced in this section. However, the CC4 software calculates stress levels far above 200 GPa. These outliers have a big influence on average values. One explanation of these unrealistic high values are the interfaces between two different phases. A look at the stress map shows that these high values occur concentrated at the grain boundaries, the interfaces of two grains or phases. Because of the two phases adding their backscatter information together at these points, Kikuchi patterns are also a summation of the two patterns and the difference is much higher than within a crystal with just some ingrain rotations for example. Still, the procedures of the OIM data collection assign these points to one of the two grains. These points have a bad confidence index (CI). The CI is attributed to each point by the OIM data collection to state the certainty of the correctness of their assignment to a certain grain. The execution of the CC4 calculation and with it the XCF finds a high value of difference between these 'double' Kikuchi patterns and the reference pattern. In order to avoid this source of error it showed to be useful to use a filter setting for all values above 30 GPa to zero. This filter eliminated mostly under 1 % of the values but never more than 3 % of the values.

4 Measurements and Results

This thesis examines the possibilities and reliability of the CC4 software, and uses it to investigate the influence of grinding processes and the magnetic saturation on the stress levels within the sample. This chapter focuses on the measurements and obtained results.

Section 4.1 shows the results of the examination of a silicon wafer. Based on the assumption of very low stress levels within the Si single crystal wafer, these measurements give an idea of the reliability of the values calculated by the CC4 software.

As visible in figure 3.4, different areas on the surface were investigated, which served different purposes. Since WC and Co phases lead to different findings, these were evaluated and are presented separately for each measurement. Section 4.2 shows the maps obtained by the measurements of the WC-Co samples. All investigated WC-Co samples are noted in table 4.1. Section 4.2.1 presents the results serving the analysis of the Co phase of the cemented carbide samples. The aim of this section is to get an impression of the influence of the magnetic saturation on residual stress levels within the Co phase. To get a better understanding of the influence of the magnetic saturation and with it the dissolved C amount in the Co phase on the residual stress levels, within the Co, the Co phase is analysed directly on the surface and within the bulk of the sample. Also the influence of surface treatment on the Co phase directly on the surface is analysed. Section 4.2.2 gives an idea of the influence of surface treatment on the residual stress levels within the WC grains directly at the surface.

To get an idea of the comparability of the EBSD results, a XRD analysis was executed on the WC-Co samples. These results are presented in the last section of this chapter (section 4.2.3).

4.1 Calibration Measurements

4.1.1 Silicon Wafer Measurements

To evaluate the reliability of the values calculated by the CC4 software, the stress levels within a silicon wafer were analysed. The assumption was, that there should be no residual stress within a silicon wafer. Therefore, the expectation was to find close to zero stress levels for σ_{11} and σ_{VM}. Under 0.1 GPa would be acceptable, taking measured stress levels of far more than 1 GPa into account. The measured area of $1x1$ mm^2 is far bigger than the recommended value of $150x150$ μm^2 by the CC4 software. In figure 4.1 the measured residual stress of the silicon sample is displayed with (σ_{VM}: figure 4.1b) and without (σ_{VM}: figure 4.1a) beam shift correction to demonstrate the effect of the beam shift correction on the results. The range of the uncorrected von Mises stress is 0 GPa to 4.53 GPa with mean σ_{VM} stress of 2.31 GPa. With correction, the maximum value for the von Mises stress is 0.46 GPa. The corrected mean stress value is calculated to 0.22 GPa.

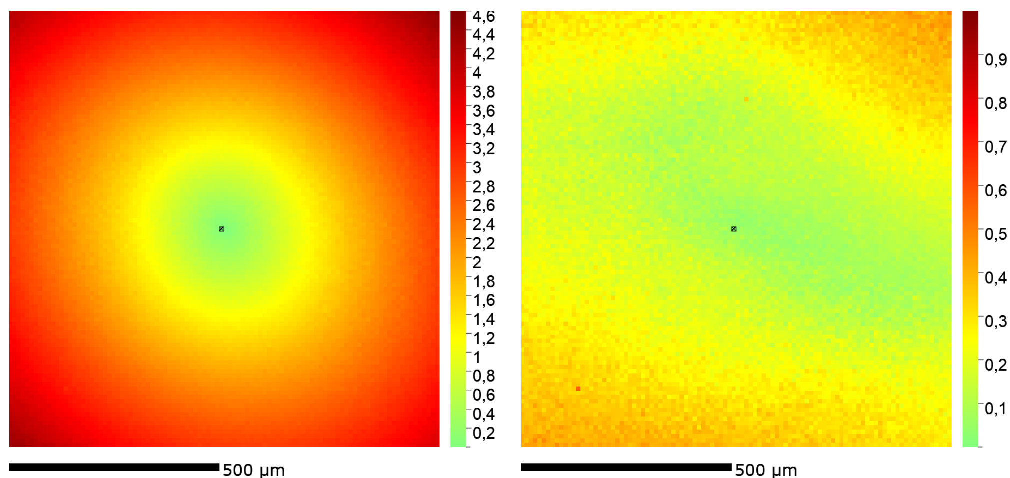

(a) σ_{VM} stress without beam shift correction. Scale limited to 4.6 GPa.

(b) σ_{VM} stress beam shift corrected. Scale limited to 1 GPa.

Figure 4.1: σ_{VM} stress maps for a silicon wafer calculated with and without beam shift correction

4.2 WC-Co Samples

EBSD measurement techniques offer the possibility to analyse very small areas, and therefore give an idea of how the WC grains are arranged within the Co binder phase. It is possible to analyse residual type III stress within the Co phase and within single WC grains. As mentioned before, the measurement of the WC-Co samples investigated the influence of the magnetic saturation and of the surface treatment on the residual stress levels. For this evaluation, six measurements were executed on four samples. Surface cross sections of samples with high magnetic saturation and low magnetic saturation were investigated. For both high and low magnetic saturation the surface cross sections were executed on a sample with untreated surface and one with surface treatment. Also a bulk cross section of a sample with high magnetic saturation and one with low magnetic saturation were measured. The parameters of the measurements are displayed in table 4.1. The position of the investigated areas is sketched in figure 3.4.

Table 4.1: Parameters of the excuted measurements and samples

	Center cross section Stepsize 100 nm	Surface cross section untreated Stepsize 200 nm	Surface cross section ground Stepsize 200 nm
Low magnetic saturation	$12x12\ \mu m^2$ figure 4.6 Co: section 5.2.3 WC: section 5.3.3	$20x20\ \mu m^2$ figure 4.4 Co: section 5.2.2 WC: section 5.3.2	$20x20\ \mu m^2$ figure 4.5 Co: section 5.2.2 WC: section 5.3.2
High magnetic saturation	$12x12\ \mu m^2$ figure 4.7 Co: section 5.2.3 WC: section 5.3.3	$20x20\ \mu m^2$ figure 4.2 Co: section 5.2.1 WC: section 5.3.1	$20x20\ \mu m^2$ figure 4.3 Co: section 5.2.1 WC: section 5.3.1

The obtained maps are shown in figures 4.2 (high magnetic saturation, untreated surface), 4.3 (high magnetic saturation, ground surface), 4.4

(low magnetic saturation, untreated surface), 4.5 (low magnetic saturation, ground surface), 4.6 (low magnetic saturation, bulk cross section) and 4.7 (high magnetic saturation, bulk cross section).

The IPF maps are presented in figures 4.2a (high magnetic saturation, untreated surface) 4.3a (high magnetic saturation, ground surface), 4.4a (low magnetic saturation, untreated surface), 4.5a (low magnetic saturation, ground surface), 4.6a (low magnetic saturation, bulk cross section) and 4.7a (high magnetic saturation, bulk cross section). These maps indicate the orientation of the crystals with a colour according to their Miller indices.

The IQ maps give an idea of the quality of the captured Kikuchi patterns of a measurement. These maps are shown in figures 4.2d (high magnetic saturation, untreated surface) 4.3d (high magnetic saturation, ground surface), 4.4d (low magnetic saturation, untreated surface), 4.5d (low magnetic saturation, ground surface), 4.6d (low magnetic saturation, bulk cross section) and 4.7d (high magnetic saturation, bulk cross section).

Results concerning the Co phase and the WC phase are presented in section 4.2.1 and 4.2.2.

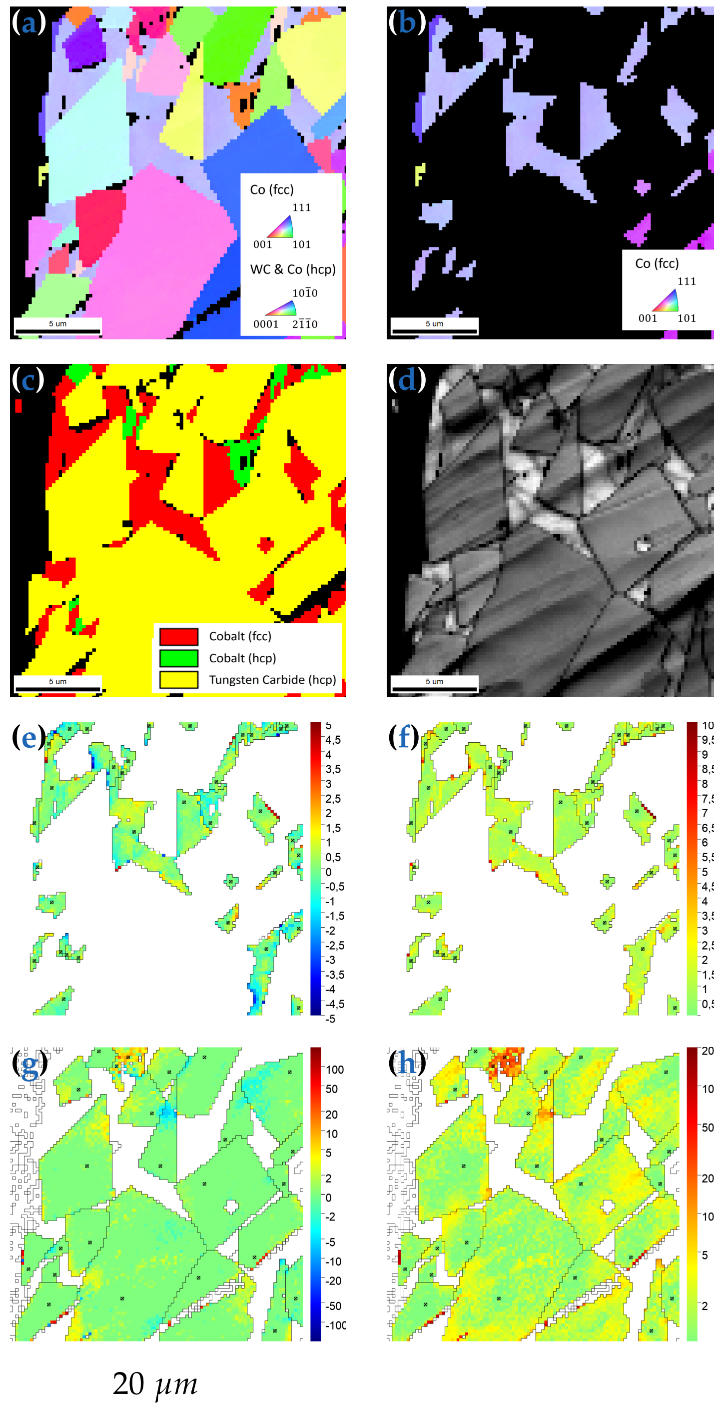

Figure 4.2: Surface cross section of a sample with high magnetic saturation and untreated surface: IPF(a), IPF Co(fcc)(b), Phase map(c), IQ(d), $Co\ \sigma_{11}$(e), $Co\ \sigma_{VM}$(f), $WC\ \sigma_{11}$(g), $WC\ \sigma_{VM}$(h)

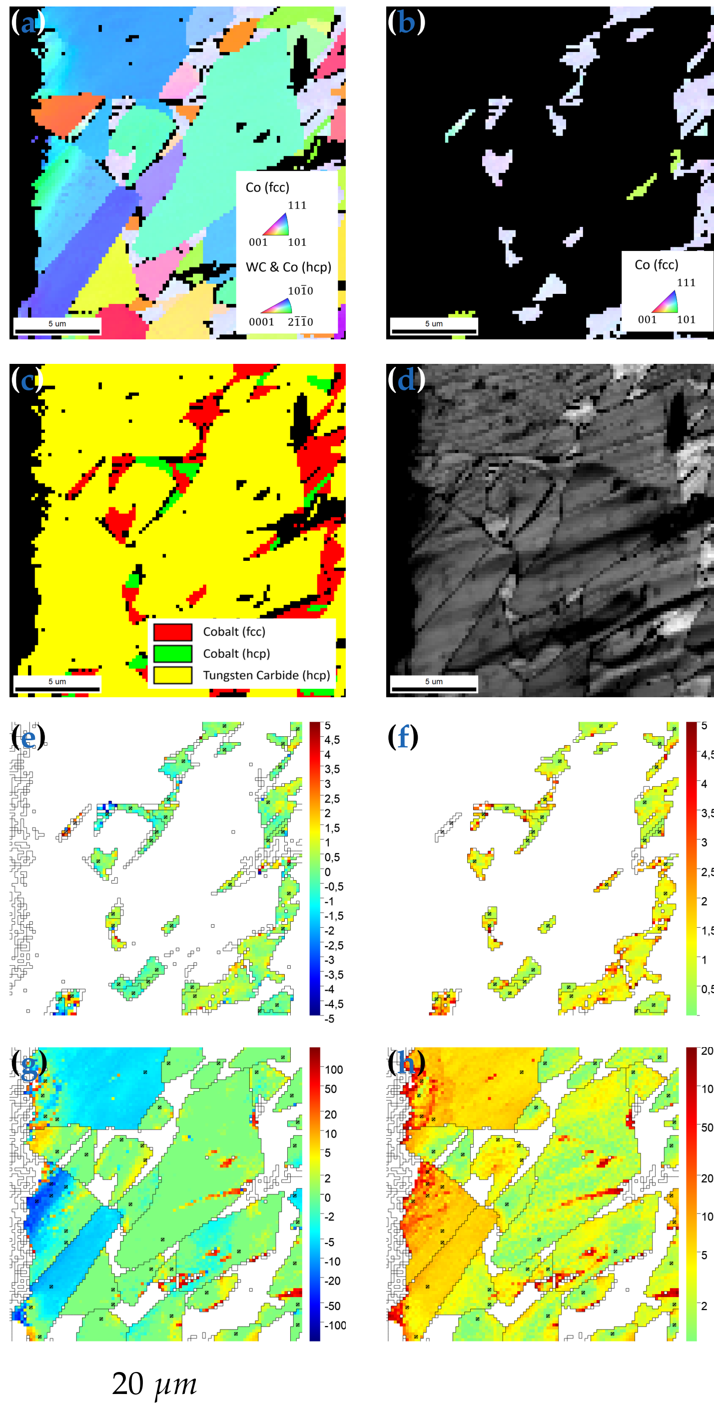

Figure 4.3: Surface cross section of a sample with high magnetic saturation and ground surface: IPF(a), IPF Co(fcc)(b), Phase map(c), IQ(d), $Co\ \sigma_{11}$(e), $Co\ \sigma_{VM}$(f), $WC\ \sigma_{11}$(g), $WC\ \sigma_{VM}$(h)

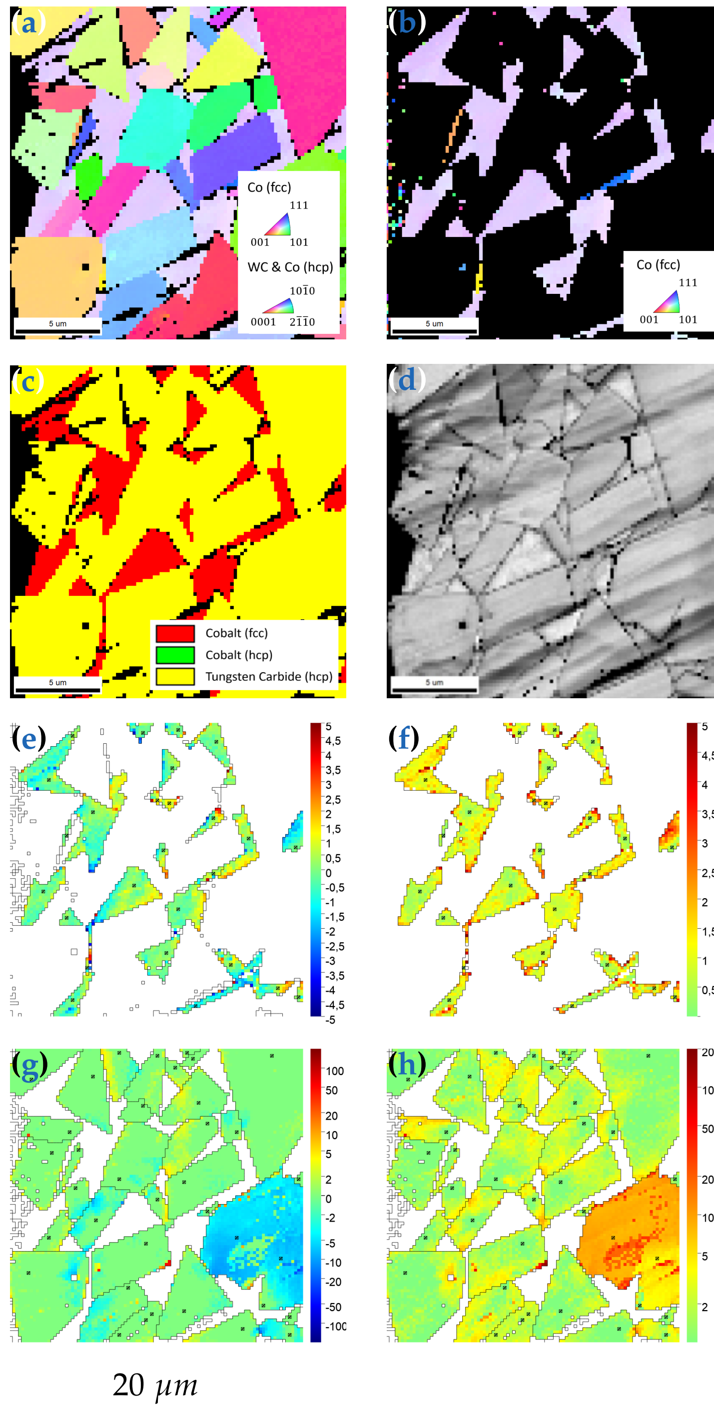

Figure 4.4: Surface cross section of a sample with low magnetic saturation and untreated surface: IPF(a), IPF Co(fcc)(b), Phase map(c), IQ(d), $Co\ \sigma_{11}$(e), $Co\ \sigma_{VM}$(f), $WC\ \sigma_{11}$(g), $WC\ \sigma_{VM}$(h)

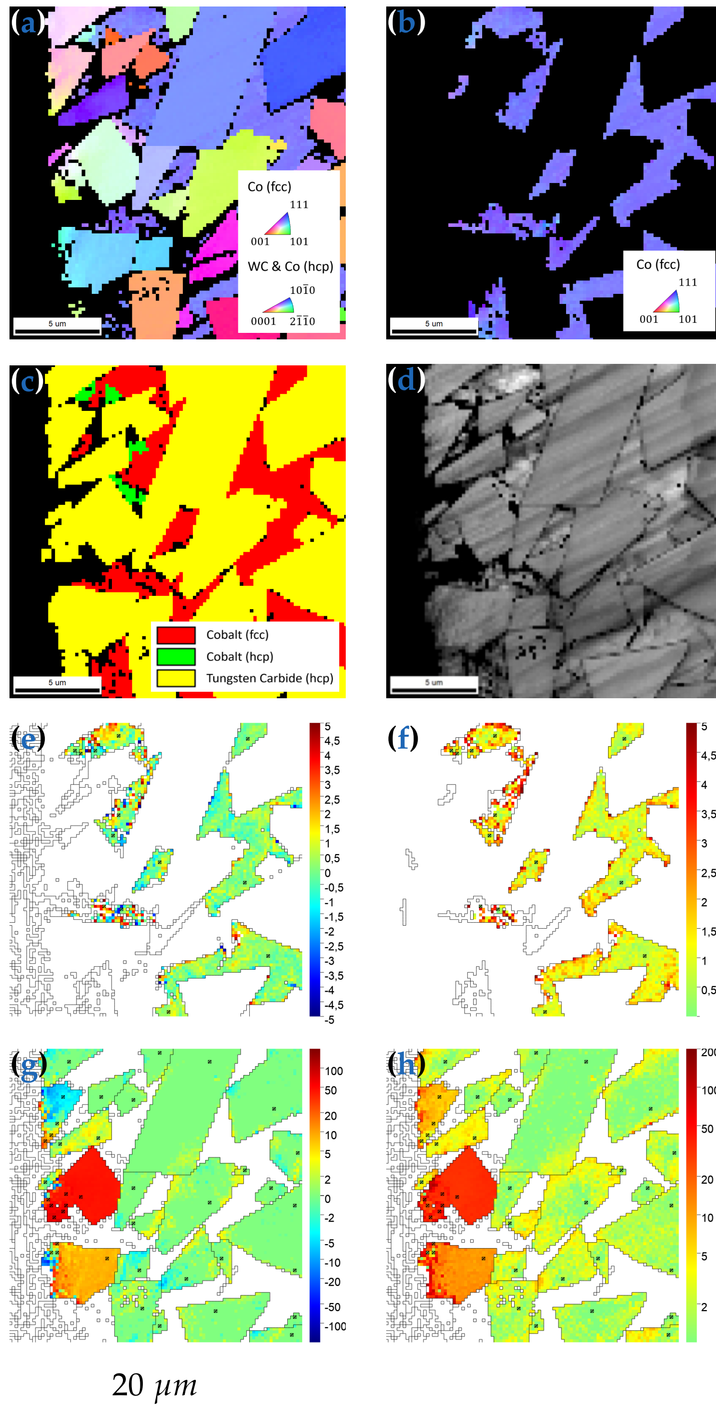

Figure 4.5: Surface cross section of a sample with low magnetic saturation and ground surface: IPF(a), IPF Co(fcc)(b), Phase map(c), IQ(d), *Co* σ_{11}(e), *Co* σ_{VM}(f), *WC* σ_{11}(g), *WC* σ_{VM}(h)

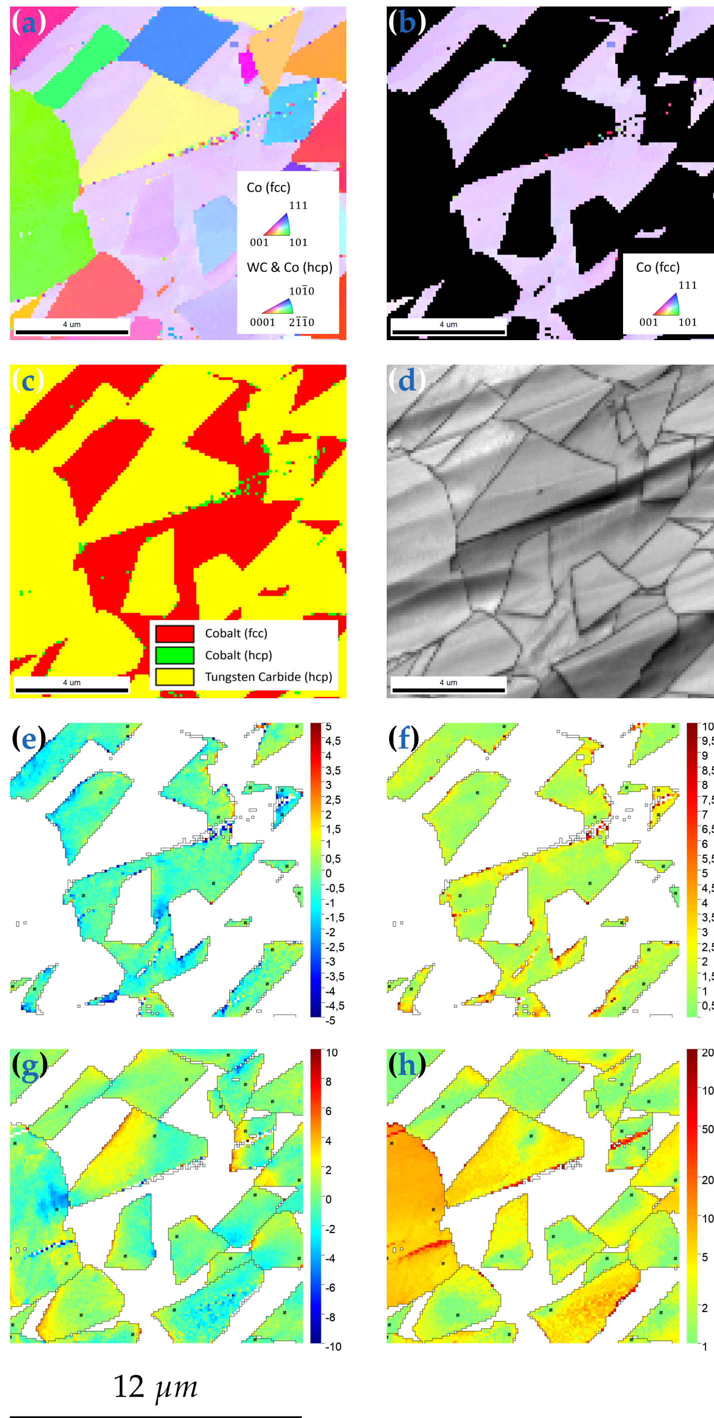

Figure 4.6: Bulk cross section of a sample with low magnetic saturation: IPF(a), IPF Co(fcc)(b), Phase map(c), IQ(d), *Co* σ_{11}(e), *Co* σ_{VM}(f), *WC* σ_{11}(g), *WC* σ_{VM}(h)

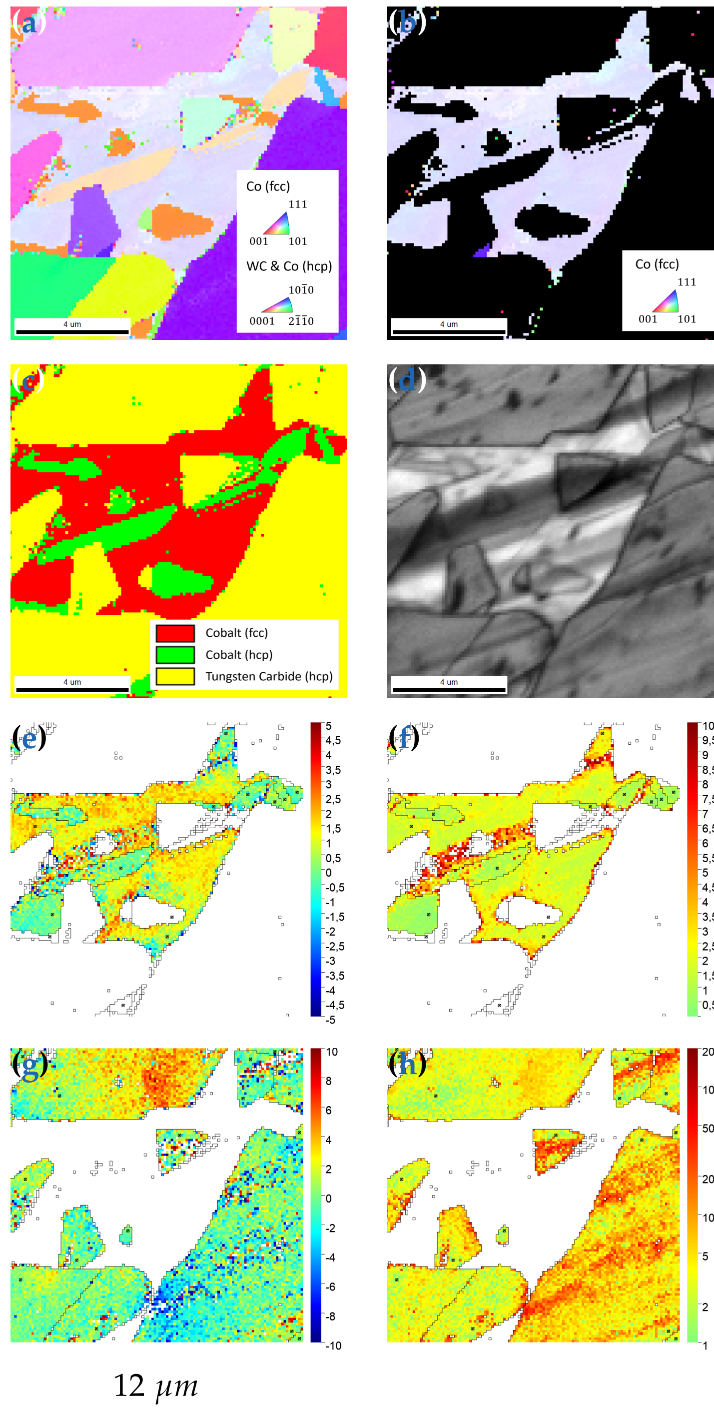

Figure 4.7: Bulk cross section of a sample with high magnetic saturation: IPF(a), IPF Co(fcc)(b), Phase map(c), IQ(d), $Co\ \sigma_{11}$(e), $Co\ \sigma_{VM}$(f), $WC\ \sigma_{11}$(g), $WC\ \sigma_{VM}$(h)

4.2.1 Results of the Co phase (influence of the magnetic saturation and stress on the Co phase)

This section presents the influence of the magnetic saturation on the stress levels within the Co phase. The amount of the W and C atoms in the Co binder phase influences the magnetic saturation. The effect of these impurity atoms on the residual stress is examined. Also the influence of grinding processes on stress levels on the surface is studied with these results. Results of the Co phase of surface cross sections with high and low magnetic saturation and ground and untreated surfaces and for bulk cross sections with high and low magnetic saturation are presented. The corresponding maps are displayed in figures 4.2(a - f), 4.3(a - f), 4.4(a - f), 4.5(a - f), 4.6(a - f) and 4.7(a - f). An overview of the obtained values is given in table 4.2. The results are discussed in section 5.2.

The IPF maps of the Co phase in fcc are presented in figures 4.2b (high magnetic saturation, untreated surface) 4.3b (high magnetic saturation, ground surface), 4.4b (low magnetic saturation, untreated surface), 4.5b (low magnetic saturation, ground surface), 4.6b (low magnetic saturation, bulk cross section) and 4.7b (high magnetic saturation, bulk cross section). This phase is present in mostly just one single orientation over the whole area, recognizable by the single colour of these grains. Mingard et al.[37] found very large Co binder grains.

The phase maps of the samples with high magnetic saturation or ground surface show an additional presence of Co in hcp structure. This additional Co is present over the whole area in phase maps 4.2c (high magnetic saturation, untreated surface), 4.3c (high magnetic saturation, ground surface) and 4.7c (high magnetic saturation, bulk cross section). Figure 4.5c (low magnetic saturation, ground surface) indicates Co hcp grains directly on the ground surface. In figures 4.4c (low magnetic saturation, untreated surface) and 4.6c (low magnetic saturation, bulk cross section) no Co hcp phase is indicated.

The Co mean stress value from the sample with high magnetic saturation and untreated surface within the XRD comparison region is calculated to

1.32 GPa for σ_{VM} stress from figure 4.2f and 0.09 GPa for σ_{11} stress from figure 4.2e.

The XRD comparison region is based on the assumption of the penetration depth of x-rays into WC-Co material. Simulations calculated this depth to about 3 μm. Also an XRD stress measurement gives an average stress value over a bigger area, of at least 500x500 μm^2. Therefore the XRD comparison region values are mean stress values of the values from the surface up to the depth of 3 μm. Comments about the comparability of EBSD and XRD analysis can be found in section 5.4.

Also for the samples with high magnetic saturation and ground surface the average stress values within the XRD comparison region was calculated and the stress maps are displayed. The von Mises stress of the cobalt phase was calculated to 4.23 GPa from figure 4.3f, the average σ_{11} stress was calculated to -1.43 GPa from figure 4.3e.

The samples with low magnetic saturation show similar trends. The average von Mises stress value over the XRD comparison region in the Co phase of the sample with untreated surface is calculated to 1.20 GPa from the von Mises stress map (figure 4.4f). In the same region the average σ_{11} stress for the Co phase is -0.20 GPa (figure 4.4e). The sample with ground surface has an average Co von Mises stress value of 5.36 GPa (figure 4.5f), the σ_{11} stress values is 0.24 GPa (figure 4.5e).

The measurements of the bulk cross sections were far enough in the bulk, so the surface did not influence the results. They have similar properties to the untreated surface cross section with the corresponding magnetic saturation. The Co average von Mises stress over the whole area of the bulk cross section with low magnetic saturation is calculated to 1.65 GPa from the von Mises stress map (figure 4.6f). The average σ_{11} stress for the Co phase is -0.63 GPa (figure 4.6e). Within the sample with high magnetic saturation the average von Mises stress was calculated to 2.70 GPa from the von Mises map (figure 4.7f) and to 0.66 GPa from the σ_{11} map (figure 4.7e).

Especially the von Mises stress directly at the surface of the samples with ground surface show significantly higher values with 4.23 GPa (high magnetic saturation) and 5.36 GPa (low magnetic saturation). The

samples with untreated surface shows lower stress levels of 1.20 GPa (high magnetic saturation) and 1.32 GPa (low magnetic saturation). A similar behaviour for the σ_{11} could not be observed. The stress values within the bulk cross sections do not show a significant difference. An overview of the obtained values is given in table 4.2.

Table 4.2: Calculated values for the Co phase within the first 3 μm from the surface

$\overline{\sigma_{VM}}$ average von Mises stress
$\overline{\sigma_{11}}$ average σ_{11} stress

	High magnetic saturation		
Sample	$\overline{\sigma_{VM}}$ / GPa	$\overline{\sigma_{11}}$ / GPa	crystal structure
Untreated surface	1.32	0.09	fcc & hcp
Ground surface	4.23	-1.43	fcc & hcp

	Low magnetic saturation		
Sample	$\overline{\sigma_{VM}}$ / GPa	$\overline{\sigma_{11}}$ / GPa	crystal structure
Untreated surface	1.20	-0.20	fcc
Ground surface	5.36	0.24	fcc & hcp

	Bulk cross section (Calculated over the whole measured area)		
Sample	$\overline{\sigma_{VM}}$ / GPa	$\overline{\sigma_{11}}$ / GPa	crystal structure
Low magnetic saturation	1.65	-0.63	fcc
High magnetic saturation	2.70	0.66	fcc & hcp

4.2.2 Results of the WC phase (influence of the grinding processes on the stress levels directly at the surface)

This section presents the results of the investigation of the influence of the grinding processes on the residual stress levels within the WC grains

directly at the surface. Values were calculated for surface cross sections with high and low magnetic saturation and ground and untreated surfaces and for bulk cross sections with high and low magnetic saturation. The corresponding maps are displayed in figures 4.2(a, c, d, g and h), 4.3(a, c, d, g and h), 4.4(a, c, d, g and h), 4.5(a, c, d, g and h), 4.6(a, c, d, g and h) and 4.7(a, c, d, g and h). The obtained values are displayed in table 4.3. The findings are discussed in section 5.3.

The mean von Mises stress of the WC phase of the sample with high magnetic saturation and untreated surface is 1.54 GPa within the XRD comparison region, calculated from the von Mises stress map (figure 4.2h). The mean σ_{11} stress in the same region averages to 0.27 GPa taken from the stress map in figure 4.2e. The average von Mises stress of WC of the sample with ground surface was calculated to 6.44 GPa from figure 4.3h and the σ_{11} stress in figure 4.3g averages to 1.49 GPa.

The average von Mises stress value in the WC phase of the sample with low magnetic saturation and untreated surface in the XRD comparison region is 1.38 GPa calculated from figure 4.4h, and the average σ_{11} stress value of 0.53 GPa is evaluated from figure 4.4g. The sample with ground surface has an average WC von Mises stress value of 4.57 Gpa (figure 4.5h). The σ_{11} stress values for the sample with ground surface is -0.29 GPa (figure 4.5g).

Also for the bulk cross section the stress values for the WC phases were evaluated. For the samples with low magnetic saturation they are 3.51 GPa (σ_{VM}: figure 4.6h) and 0.12 GPa (σ_{11}: figure 4.6g). The values for the samples with high magnetic saturation were calculated to 5.36 GPa (σ_{VM}: figure 4.7h) and 0.68 GPa (σ_{11}: figure 4.7g). In table 4.3 the calculated values are listed.

Similar as in the Co phase, regions near surface treatment show significantly higher stress values than samples without surface treatment. These higher values are 6.44 GPa (high magnetic saturation) and 4.57 GPa (low magnetic saturation). The lower values for the samples without surface treatment are 1.54 GPa (high magnetic saturation) and 1.38 GPa (low magnetic saturation). As in the Co phase, a similar behaviour could not be observed for σ_{11} values. The stress values within the bulk cross sections do not show a significant difference.

Table 4.3: Calculated values of the WC phase within the first 3 μm from the surface

$\overline{\sigma_{VM}}$	average von Mises stress
$\overline{\sigma_{11}}$	average σ_{11} stress

	High magnetic saturation	
Sample	$\overline{\sigma_{VM}}$ / GPa	$\overline{\sigma_{11}}$ / GPa
Untreated surface	1.54	0.27
Ground surface	6.44	1.49

	Low magnetic saturation	
Sample	$\overline{\sigma_{VM}}$ / GPa	$\overline{\sigma_{11}}$ / GPa
Untreated surface	1.38	0.53
Ground surface	4.57	-0.29

	Bulk cross section (Calculated over the whole measured area)	
Sample	$\overline{\sigma_{VM}}$ / GPa	$\overline{\sigma_{11}}$ / GPa
Low magnetic saturation	3.51	0.12
High magnetic saturation	5.36	0.68

4.2.3 Residual Stress Evaluation via XRD

The four WC-Co samples (low and high magnetic saturation, each with untreated and ground surface) were also examined via XRD by Ceratizit [31]. The results of the XRD evaluation are shown in table 4.4. XRD measurements only evaluate the WC phase of the sample, since the Co peaks in the diffractogram are to small. A model of the surface where the XRD measurement was carried out can be found in figure 3.5. Since XRD analyses are a well-established method for the evaluation of residual stress, these results serve as reference for the comparison of the XRD and EBSD values.

Table 4.4: Residual stress within the WC phase of a WC-Co sample by XRD

	Low magnetic saturation / GPa	High magnetic saturation / GPa
Untreated suface	-0.363 ± 0.040	-0.200 ± 0.036
Ground surface	-2.203 ± 0.077	-1.806 ± 0.053

5 Discussion

This chapter discusses the results of chapter 4. Section 5.1 looks at the reliability of the values obtained by the CC4 software through evaluation of the results of the Si wafer, and discusses influences and the magnitude of measurement uncertainties.

Section 5.3 evaluates the results of the WC grain analysis for high and low magnetic saturations and for ground and untreated surfaces. The calculations and recognitions from the Co phase can be found in section 5.2.

Section 5.4 tries to compare the values obtained in this present work with values gained by a measurement of the well-established XRD analysis and examines the problems of these comparisons.

The last section of the chapter, section 5.5, gives an overview over the obtained values and states reference values and literature values.

5.1 Preliminary Considerations

5.1.1 Silicon Wafer

The idea of the silicon wafer measurements was to evaluate the reliability of the values of the CC4 software. A silicon wafer was chosen because there is no significant residual stress known within a silicon wafer. Also Villert et al. [38] used a silicon wafer to evaluate the accuracy of EBSD strain measurement with the assumption of an unstrained center point of the measurement, with the wafer bent around the center. Another aim of these measurements was to evaluate how the CC4 software deals with

bigger areas, so the evaluated area is $1x1\ mm^2$. Figure 5.1 shows the σ_{11} and the σ_{VM} mean stress profile of the analysed silicon wafer, calculated as mentioned in section 3.5.5. According to the assumption of a nearly stress-less sample, average values of more than 0.1 GPa (σ_{VM}) at the edge of the area seem high (figure 5.1b). Also the span of the σ_{11} calculations of average values of about $-0.1\ GPa$ to $0.1\ GPa$ are higher than expected. However, according to the software support, CC4 is suited to examine areas of $150x150\ \mu m^2$. Therefore an area of this measurement around the reference pattern of $160x160\ \mu m^2$ was calculated separately. The results are displayed in figure 5.2. Within this reduced area, the calculated values for the σ_{11} stress values are between $-0.07\ GPa$ and $0.06\ GPa$ (figure 5.2b). Within stress measurements up to several GPa or higher these values are negligible. The σ_{VM} values however are up to $0.18\ GPa$ (figure 5.2b). Only the reference pattern has a value of zero, the next higher value is at $0.07\ GPa$. All 16 values (except the value of the reference pattern) of the calculation of the σ_{VM} stress are between $0.07\ GPa$ and $0.10\ GPa$. The value of the reference pattern is defined as zero. The calculation of the σ_{VM} stress leads to a high difference for the values directly around the reference pattern. In areas with low stress levels, values of $0.1\ GPa$ do not disappear within the measurement noise, which can lead to problems with evaluating the σ_{VM} stress. The σ_{11} stress value next to the reference pattern is calculated to $0.00013\ GPa$, so this seems to be no difficulty with σ_{11} stress evaluations. Comparing the mean stress profile graph of the whole area in figure 5.1a and of the reduced area in figure 5.2a shows the occurrence of higher stress values at larger distances from the reference pattern. This is also visible in the corresponding stress maps in figure 5.2c and figure 5.2d for σ_{VM} and σ_{11} respectively. An overview over the maximum, minimum and mean values of the $160x160\mu m^2$ section from the center of this measurement is given in table 5.1. The obtained values lie within the expected range. Given the difference between the reference pattern and the next neighbour, absolute values show stress trends within the material. To make exact evaluation of the absolute values more reliable, further research is necessary.

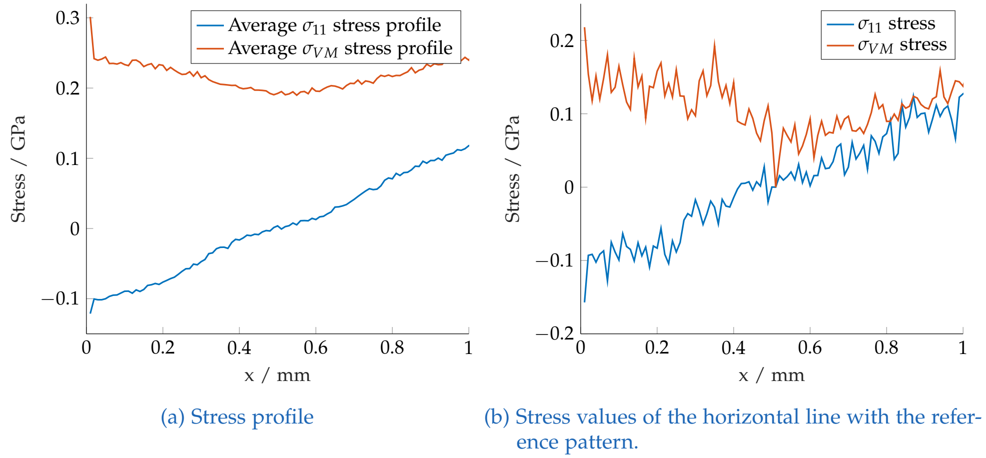

(a) Stress profile

(b) Stress values of the horizontal line with the reference pattern.

Figure 5.1: Stress values of a $1x1$ mm^2 area of a silicon wafer. The corresponding stress maps are displayed in figure 4.1b (σ_{VM}) and 5.2d (σ_{11}). The calculation of the stress profile is explained in section 3.5.5. Figure 5.1b shows the values along one line in x direction of the measurement. The displayed line is the line with the reference pattern.

Table 5.1: Values of the residual stress evaluation in an area of $160x160$ μm^2 of a Si single crystal wafer

$\overline{\sigma_{VM}}$ average von Mises stress
$\overline{\sigma_{11}}$ average σ_{11} stress

	$\overline{\sigma_{VM}}$ / GPa	$\overline{\sigma_{11}}$ / GPa
Minimum value	0.00	-0.07
Maximum value	0.18	0.06
Span	0.18	0.13
Mean stress	0.09	0.008

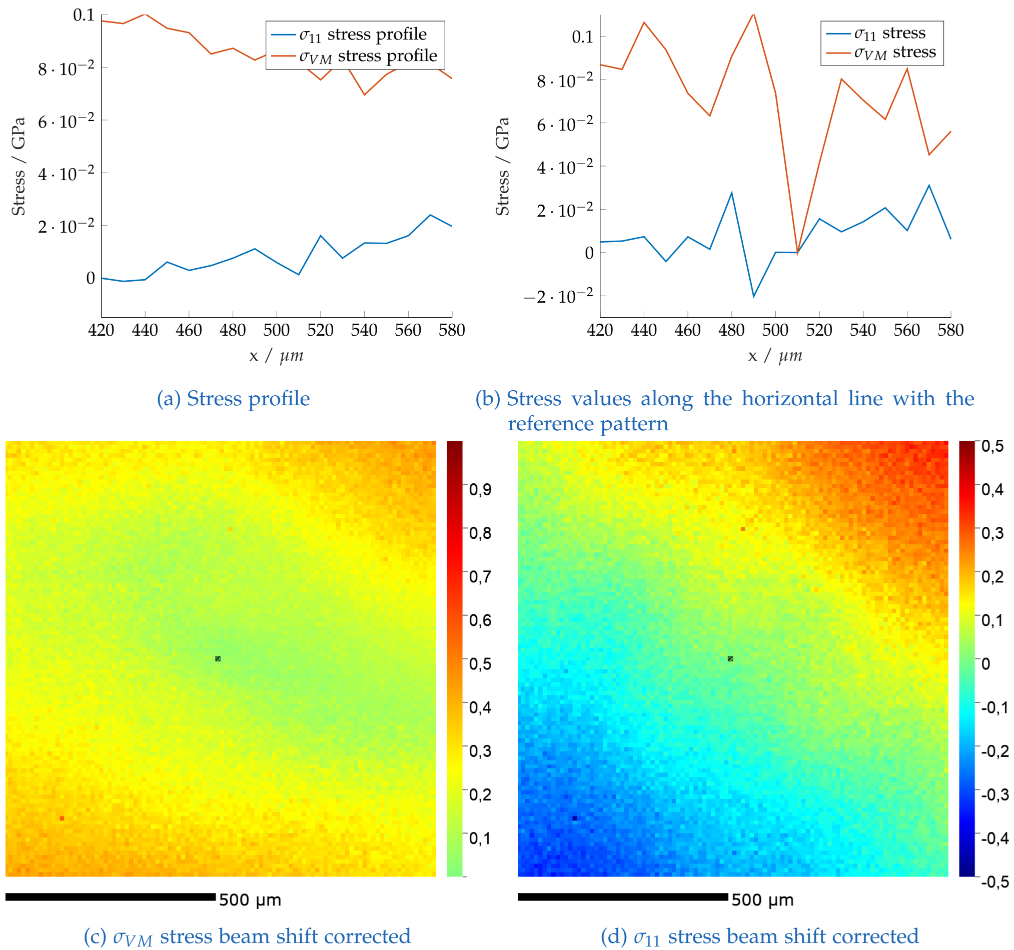

(a) Stress profile

(b) Stress values along the horizontal line with the reference pattern

(c) σ_{VM} stress beam shift corrected

(d) σ_{11} stress beam shift corrected

Figure 5.2: Stress values of a $160x160\ \mu m^2$ area of a silicon wafer. The corresponding stress maps are displayed again. The stress profile and the horizontal line are calculated for a section of $160x160\ \mu m^2$ from the centre of the measurement.

5.1.2 Influence of Grooves on the Surface

One of the problems not yet overcome is the curtaining effect, which results from grooves on the surface due to ion polishing. The curtaining effect depends on the hardness of the material, the glue and the grain size, and affects the Kikuchi pattern as a result of the uneven surface. At surface edges within one grain, different orientations are measured. Grooves can also result in a slow change of orientation, which causes the software to treat this area like a small rotation within the grain and therefore an area with high stress and strain levels. In order to keep the impact of the curtaining effect as small as possible, smooth areas on the surface were chosen, found by their impression in the SE image. In particular, our samples consist of hard WC grains and soft Co in between. The grooves are mainly located in the Co areas. These samples were mounted to the blade with conductive silver to protect the cobalt areas. While hardening, the conductive silver forms silver flakes. These little flat constructs of silver are between sample and blade and hold them together. At the ion polishing process these silver flakes seem to be more protective for the Co areas than super glue, resulting in smoother edges directly at the surface at the cross section. This method was especially useful for WC-Co samples. A little curtaining effect was observed despite using conductive silver.

In order to further minimize the curtaining effect, one could either use a blade with a very stable edge (e.g. diamond), a harder glue, or a rotation during polishing. In this work we did not have access to these possibilities.

5.1.3 Measurement Uncertainty and Absolute Values

Evaluation by the CC4 yields stress maps with absolute values. The description of the uncertainty of these values varies from author to author [27][24][38][39]. A perfect, stress-free sample does not exist, therefore, the uncertainty can only be estimated. This section gives some ideas how big the error could be by analysing different aspects of the results.

Sources of errors are manifold. First of all, the preparation can damage the grains, and especially create grooves on the surface, which leads to rough surfaces and areas of bad IQ. The size of the groove depends on several factors like the size of the WC grains, the glue or the blade. The height of the grooves can reach a maximum of some 100 nm. Near the surface is a region of higher stress levels due to surface treatment. The IQ can also be negatively affected by contamination effects. Long exposure to the electron beam leads to deposits on the surface which are degrading the Kikuchi pattern quality. Binning effects lead to smaller Kikuchi patterns and therefore to less precise results. A compromise between size of the Kikuchi pattern and exposure time, due to contamination problems, was found in $2x2$ binning.

The choice of reference pattern has an influence on the results as demonstrated in section 3.5.3.

Calculating mean stress values has the disadvantage of losing information, in exchange for a better overview. This averaging also leads to values which are difficult to analyse in terms of their significance, especially with directional values like the σ_{11} stress. This is visible in figure 5.8a below. The mean stress value for the sample with the ground surface is -0.29 GPa, the sample with the untreated surface has an average value of 0.53 GPa. A look at the graph, which also plots mean values, shows that the sample with the ground surface, has positive and negative values, whereas the sample with the untreated surface features only positive values. The graph leads to the expectation of a higher stress level within the sample with ground surface. Taking this into account, a compromise was made between simplifying the results and not losing their significance.

For further error analysis, seven σ_{VM} measurements of an untreated surface cross section of a sample with high magnetic saturation were examined. The measurements were executed on two samples with the same properties and to overcome contamination problems, on different areas along the surface. All of the measurements have the same settings as the measurement of the sample with the untreated surface and high magnetic saturation in section 4.2. The mean stress values within the first 3 μm from the surface are displayed in table 5.2. The results are all between 1.50 GPa and 2.20 GPa. Also taking the σ_{VM} results of table 4.2

Table 5.2: Mean stress value of the WC phase within the first 3 μm from the surface of a sample with high magnetic saturation with untreated and ground surface

$\overline{\sigma_{VM}}$ average von Mises stress

$\overline{\sigma_{VM}}$ / GPa (untreated surface)	$\overline{\sigma_{VM}}$ / GPa (ground surface)
1.67	5.18
1.70	6.44
2.20	5.50
1.51	
2.20	
1.50	
2.07	

and 4.3 into account, this gives a span for the stress values of the sample with the untreated surface (WC) of 1.20 GPa to 2.20 GPa. Therefore one can assume average stress values for σ_{VM} to 1.70 $\pm$ 0.50 GPa for areas with low stress levels. This means an uncertainty of 30 %.

The analysis of three measurements with ground surface resulted in values between 5.18 GPa and 6.44 GPa. Three surface cross sections of a sample with ground surface were examined. The properties of the sample and the settings of the measurements were the same as for the sample with high magnetic saturation and ground surface in section 4.2. Also with respect to the results in table 4.2 and 4.3, and the assumption of an uncertainty of 30 %, this would lead to an assumption of high σ_{VM} average stress values of about 5 $\pm$ 1.5 GPa. The results of the XRD measurements in table 4.4 are much lower than the values obtained by EBSD evaluations.

Analysing the WC grains within the earlier mentioned seven σ_{VM} measurements of an untreated surface cross section of the sample with high magnetic saturation gives the results visible in figure 5.3. These results suggest a much wider span for the stress values measurable in this sam-

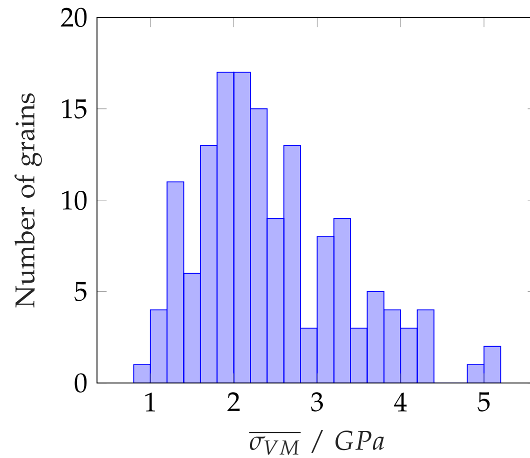

Figure 5.3: Mean σ_{VM} stress of the grains

ple. $\overline{\sigma_{VM}}$ stress values are spanning from below 1 GPa to up to higher than 5 GPa. Within these seven measurements taken for this evaluation, 150 WC grains were evaluated with an average number of 296 measurement points, and between 10 and 2102 measurement points per grain.
The values obtained from the CC4 software very well reflect the stress within the material. Areas with higher stress levels are clearly distinguishable from areas with lower stress levels. The quantitative results are affected by some uncertainties within a not too wide margin of error. For enhanced results and thus an improved understanding of the the reliability of the values obtained by the CC4 software further investigations are necessary. This goes beyond the scope of the present work. Summarizing it can be stated, that the obtained values follow the expected trends of high and low stress values. From the experiments carried out within this study, an upper error bound of 30 % may be deduced for the von Mises stress determination.

5.2 Residual Stress Evaluation Within the Co Phase of a WC-Co sample

In this section the influence of surface treatment on the Co phase and the influence of the amount of C in the WC phase is analysed. A higher amount of C within the WC phase leads to a higher amount of C dissolved in the C binder. However, this results in high or low magnetic saturation. The assumption leading to this evaluation was that a higher carbon level within the sample with high magnetic saturation would show a higher stress level due to the impurities in the Co binder caused by the carbon atoms. Furthermore it was also assumed that samples with surface treatment would show higher stress levels within the WC- and the Co-phase. The analysis of the surface treatment's influence was done with respect to the depth of the measured area. The influence of surface treatment was supposed to affect just the surface grains and the cobalt at a maximum of one WC-grain in depth. The average grain size of the coarse grain WC-Co samples investigated in this thesis is 6 μm. The calculation of the mean stress profiles is explained in section 3.5.5.

5.2.1 Sample With High Magnetic Saturation

Figure 5.4 shows the σ_{11} (figure 5.4a) and the σ_{VM} (figure 5.4b) mean stress profile for a sample with high magnetic saturation. The σ_{VM} graph shows the same difference between the sample with ground and untreated surface within the first 3 μm as in the WC phase. Also the calculated values from table 4.2 of 1.32 GPa for the sample with untreated surface and 4.23 GPa for the sample with ground surface lie in the same region as the values from the WC phase for $\overline{\sigma_{VM}}$. The values of 0.09 GPa for the untreated sample and -1.43 GPa for the ground sample are also very similar to the WC values for $\overline{\sigma_{11}}$. In samples with high magnetic saturation, Co is present in fcc and hcp phase in the whole measured area (figure 4.2c and figure 4.3c).

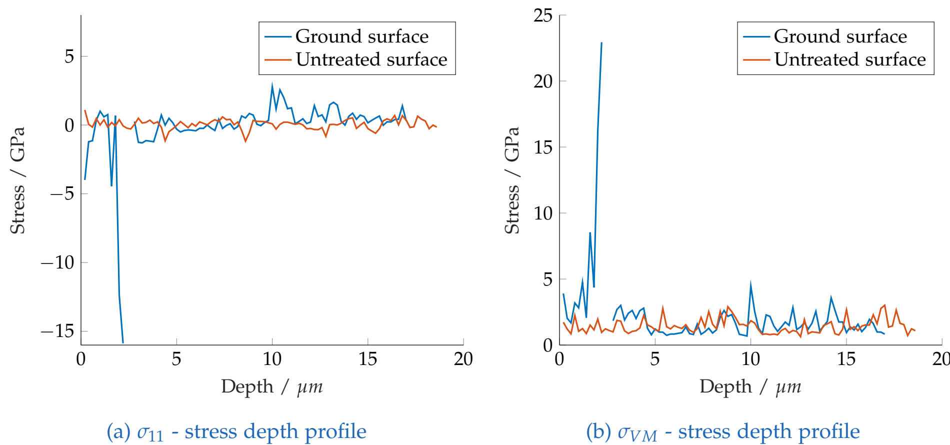

(a) σ_{11} - stress depth profile

(b) σ_{VM} - stress depth profile

Figure 5.4: Co stress depth profile of a surface cross section of sample with high magnetic saturation

5.2.2 Sample With Low Magnetic Saturation

The mean stress profile within the Co for the sample with low magnetic saturation is visible in figure 5.5. Figure 5.5a shows the depth mean σ_{11} stress and figure 5.5b the depth mean σ_{VM} stress. In the σ_{VM} graph there is higher stress visible in the sample with ground surface within the first 8 μm. Also the calculated σ_{VM} value for the XRD comparison region of 3 μm is with 5.36 GPa (table 4.2) significantly higher than 1.20 GPa for the untreated sample. Comparing the IQ-maps (untreated: figure 4.4d and ground: figure 4.5d) shows a better pattern quality for the sample with the untreated surface. So one source for the high values within the sample with ground surface is the lower image quality. The graph for the σ_{11} stress shows the same difference between the two samples, and within the sample with ground surface higher stress values could be measured. Within the samples with low magnetic saturation Co is mostly present in fcc phase (figure 4.4c). The sample with the ground surface shows presence of Co in fcc phase but within 6 μm from the surface, the region expected to be affected by surface treatment also in hcp phase (figure 4.5c).

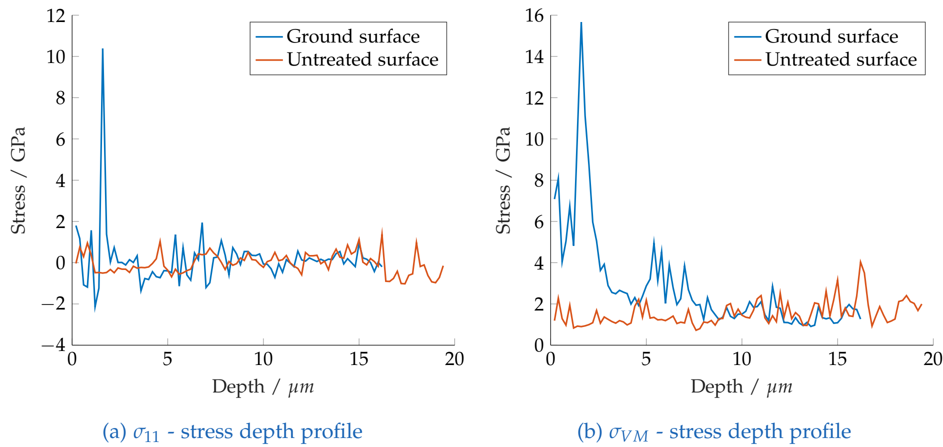

(a) σ_{11} - stress depth profile

(b) σ_{VM} - stress depth profile

Figure 5.5: Stress depth profile for Co of a surface cross section of sample with low magnetic saturation

5.2.3 Bulk Cross Section

Within the bulk cross section (figure 5.6) the sample with high magnetic saturation shows a higher von Mises stress level (figure 5.6b) and σ_{11} stress level (figure 5.6a). Comparing the calculated von Mises values (table 4.2) for the bulk cross section supports the idea given by the data (high: 2.70 GPa, low: 1.65 GPa). The $\overline{\sigma_{11}}$-stress values have a similar absolute value (high: 0.66 GPa, low: -0.63 GPa). In these measurements also different pattern qualities could be one source of the different values for the σ_{VM} values. The measurement of the sample with high magnetic saturation (figure 4.7d) shows a worse pattern quality than the measurement of the sample with low magnetic saturation (figure 4.6d).

Summarizing the given results of the Co leads to the following conclusions: Taking into account the single orientations of the Co fcc phase (figures 4.2b, 4.3b, 4.4b, 4.5b, 4.7b and 4.6b) and a 2-D map of a 3-D sample, this leads to the speculation of a large Co-grain. Findings from the literature show that Co binder phase grains can be huge [37].

The measured stress values for samples with high and low magnetic saturation do differ from each other. Also the region affected by surface treatment shows higher stress values. However, an influence of the pat-

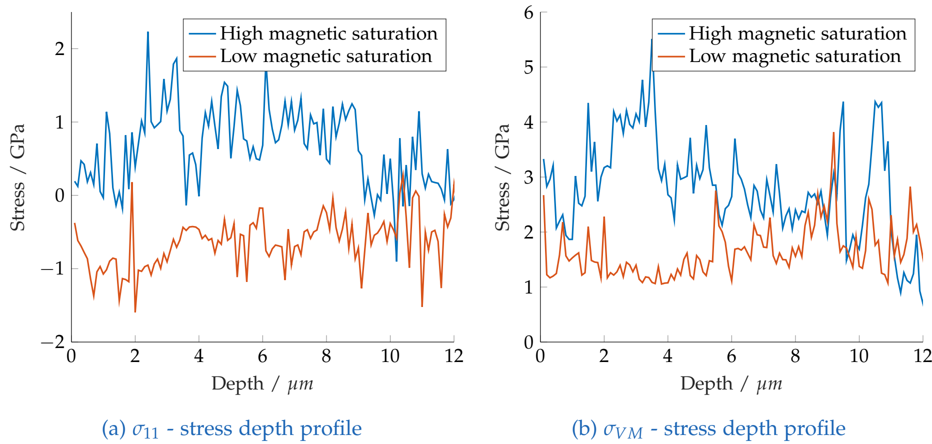

(a) σ_{11} - stress depth profile

(b) σ_{VM} - stress depth profile

Figure 5.6: Co stress profile of a bulk cross section

tern quality cannot be excluded. The expected higher stress values could be measured. The main consequence of higher magnetic saturation in the sample and also in regions affected by surface treatment is the presence of Co in fcc and hcp phase. This leads to the assumption of Co releasing high stress levels by undergoing a phase transition from fcc to hcp. The phase transition is likely because of the same packing density of the two lattice structures. Karmarkar et al. [40] could show that Co undergoes this phase transition in a carbon nano tube at a stress level of 9 GPa or more [40].

5.3 Residual Stress Evaluation Within the WC Phase of a WC-Co sample

In this section the WC of a WC-Co alloy sample is evaluated, to get an idea of the influence of surface treatment on the residual stress levels within the WC grains of the sample. The bulk cross section serves to evaluate the influence of the magnetic saturation on residual stress levels within the WC grains.

5.3.1 Sample With High Magnetic Saturation

The comparison of the stress values of a sample with high magnetic saturation with ground and untreated surface are displayed in figure 5.7. Both the σ_{11} values (figure 5.7a) and the σ_{VM} values (figure 5.7b) show a significantly higher stress for the sample with ground surface. Also the comparison of the calculated average stress values within the XRD comparison region (table 4.3) supports this suggestion. The $\overline{\sigma_{11}}$ for the untreated sample is 0.27 GPa and for the ground sample it is 1.49 GPa. The $\overline{\sigma_{VM}}$ values are 1.54 GPa (untreated surface) and 6.44 GPa (ground surface). Also the stress maps for the ground sample, figure 4.3g and figure 4.3h, show higher stress values within the first row of WC grains from the surface. In figure 4.2g and 4.2h, which are displaying the sample with untreated surfaces, do not show any difference between the stress values at the surface and the stress values in the bulk.

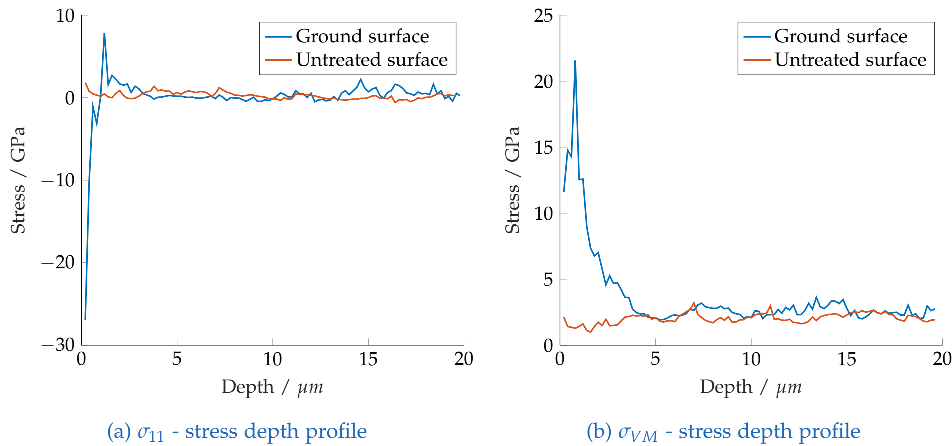

(a) σ_{11} - stress depth profile

(b) σ_{VM} - stress depth profile

Figure 5.7: Stress depth profile for WC of a surface cross section of sample with high magnetic saturation

5.3.2 Sample With Low Magnetic Saturation

The samples with low magnetic saturation are compared in figure 5.8. These measurements also show a significantly higher stress value within

the first 3 μm from the surface for samples with ground surface. For the σ_{11} stress (figure 5.8a) and for the σ_{VM} stress (figure 5.8b) the region with higher stress values is about 6 μm deep, which is about the size of one average grain. The average values for the XRD comparison region for $\overline{\sigma_{11}}$ stress were calculated to -0.29 GPa for the sample with ground surface and 0.53 GPa for the sample with untreated surface. These values are presented in table 4.3. These calculations do not take the absolute value into account, positive and negative values cancel each other out. Figure 5.8a shows a highly stressed area directly at the surface, with positive and negative values. The $\overline{\sigma_{VM}}$ values are 1.38 GPa (untreated surface) and 4.57 GPa (ground surface). Together with the visualisation of the stress in the stress maps (figures 4.5h, 4.4h, 4.5g und 4.4g) this data supports the perception that surface treatment increases the residual stress within the first layer of WC grains.

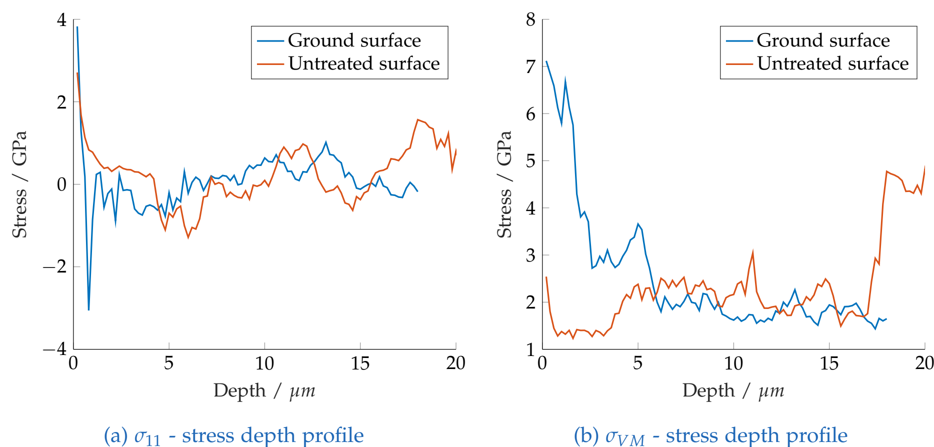

(a) σ_{11} - stress depth profile

(b) σ_{VM} - stress depth profile

Figure 5.8: Stress depth profile for WC of a surface cross section of sample with low magnetic saturation

5.3.3 Bulk Cross Section

The bulk cross section (figure 5.9) should evaluate if there are any stress value differences between high and low magnetic saturation, which could not be finally determined. The σ_{11} and the σ_{VM} values do show differences, which could originate from the difference between the pattern

qualities of the measurement of the sample with high (figure 4.7d) and low magnetic saturation (figure 4.6d). The IQ map of the sample with high magnetic saturation is darker, indicating a worse quality of the Kikuchi pattern. Therefore the calculation of the stress values is less significant, because of the nature of the XCF function. The calculated average stress values (from table 4.3) for the whole area are for the σ_{11} values 0.12 GPa (low magnetic saturation) and 0.68 GPa (high magnetic saturation) and for the σ_{VM} values 3.51 GPa (low magnetic saturation) and 5.36 GPa (high magnetic saturation). These measurements and calculations do indicate a dependence of the magnetic saturation on the stress values within the WC phase. The results of the measurements of the surface cross section of the sample without surface treatment lie in the same region for high and low magnetic saturation (table 4.3). Since these results are expected to be similar, the influence of the pattern quality cannot be completely excluded.

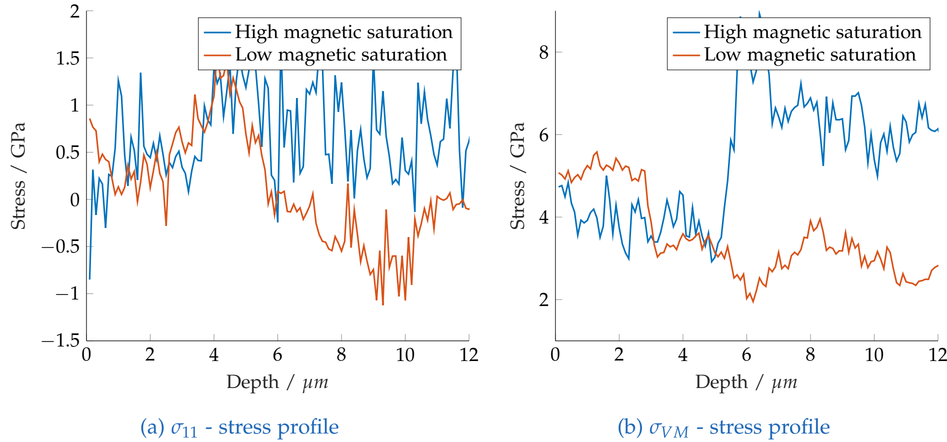

(a) σ_{11} - stress profile

(b) σ_{VM} - stress profile

Figure 5.9: Stress profile for WC of a bulk cross section

Summarizing the results of the WC phase of the WC-Co samples, a dependence of the residual stress levels directly at the surface on the grinding process could be observed. Samples with ground surface show residual von Mises stress levels between 4.5 GPa and 6.5 GPa. For samples with untreated surface, these stress levels are between 1.3 GPa and 1.6 GPa. A similar statement is not possible for σ_{11} stress levels since their vectorial nature cancels out high values when the average value is calcu-

lated. For a significant statement on the σ_{11} values, further investigation is needed.

5.4 Comparison of XRD and EBSD Measurements

One aspect of the usefulness of the CC4 software is the aspect of the results' comparability. To compare results of EBSD measurements, the samples were examined with XRD.

The comparison of stress values is oriented towards the XRD measurements. 97 % of all x-rays are diffracted within the first 3 μm under the surface. The x-ray beam has a diameter of several mm, and yields an average value for the whole area. This leads to the assumption that a rough estimation for the comparison of XRD and EBSD would be to calculate the mean value for the first 3 μm of the sample. This mean values are calculated above. As visible in table 5.3, samples with higher stress levels on the surface show higher values in the XRD and in the EBSD results. The average values for the σ_{11} stress for samples with low magnetic saturation show higher values for the sample with ground surface as well (figure 5.8a). The difference between the values for σ_{XRD} and $\overline{\sigma_{VM}}$ originate from the calculation of σ_{VM} (equation 2.4). The values for $\overline{\sigma_{11}}$ for the sample with high magnetic saturation are of the same magnitude as the σ_{XRD} values.

5.4.1 Difficulties Comparing XRD and EBSD Values

XRD and EBSD measurements yield different types of stress values as explained above (section 2.2.3). XRD yields an average value for a larger volume of about 3 μm depth and about 0.5 mm in diameter, which is referred as type I stress. In EBSD measurements type III stress values are calculated, which are relative stress changes within single grains. Jiang et al. [18] reason the problem as a consequence of the relative evaluation to a reference point. These calculated stress values cannot be further

Table 5.3: Residual stress comparison between XRD and EBSD measurements for the WC phase

σ_{XRD} x-ray diffraction (measured and calculated by Ceratizit [31])
$\overline{\sigma_{VM}}$ average von Mises stress
$\overline{\sigma_{11}}$ average σ_{11} stress

	High magnetic saturation		
	σ_{XRD} \ GPa	$\overline{\sigma_{VM}}$ \ GPa	$\overline{\sigma_{11}}$ \ GPa
Untreated surface	-0.200 ± 0.036	1.54	0.27
Ground surface	-1.806 ± 0.053	6.44	1.49
	Low magnetic saturation		
	σ_{XRD} \ GPa	$\overline{\sigma_{VM}}$ \ GPa	$\overline{\sigma_{11}}$ \ GPa
Untreated surface	-0.363 ± 0.040	1.38	0.53
Ground surface	-2.203 ± 0.077	4.57	-0.29

used to evaluate type I or type II stress due to the unknown value of the reference point. Jiang et al. [18] also suggest that type II stress values are significantly smaller than type III stress values.

5.5 Overview Over the Obtained Values and Estimation of Their Reliability

The results presented in table 5.4 summarise all values calculated within this present work and give an estimation about their meaning. The values from the literature given in table 5.4 are from simulations or experiments with different parameters than the values obtained in this present work. An exact comparison is therefore and for reasons stated in section 5.4.1 difficult and goes beyond the scope of this thesis. Yet some values are given for a better overview. The colors within the table try to give an estimation of the values' reliability based on the literature or XRD values. Green values are within respectable boundaries, yellow values

show expected trends but compared values differ a lot from each other. Large differences can originate from different experimental or material parameters. The red values do not correspond to reference values at all. Due to the relative evaluation to a reference pattern, positive or negative values are for XCF analysis a matter of convention. Therefore absolute values were compared without consideration of the sign. The deviations are summarised in the following.

The experimental values taken from Yang et al. [41] are values obtained from a cut and etched mono-like Si wafer.

A Moiré interferometry measurement of Vrinceanu and Danyluk [42] of a Si wafer states a maximum residual stress value of 1.5 MPa at the centre and zero at the boundaries.

Golovchan [43] simulated residual stress levels within the WC phase of WC-Co alloys for alloys with an amount of 20% of Co. No information on the magnetic saturation is given.

Zhu et al. [20] simulated the thermal residual stress levels within WC-Co alloys with an Co amount of 10% with the finite elements (FE) method. The von Mises values are average values. The σ_{XX} values are simulated for room temperature. No information on the magnetic saturation is given.

Table 5.4: Overview over the obtained values

$\overline{\sigma_{VM}}$	average von Mises stress (measured and calculated by the author)
$\overline{\sigma_{11}}$	average σ_{11} stress (measured and calculated by the author)
σ_{XX}	average directional stress (comparable to σ_{11} stress)
XRD	x-ray diffraction (measured and calculated by Ceratizit [31])
Properties	magnetic saturation
Surface	ground or untreated surface or bulk cross section for surface cross sections the calculated values for the XRD comparison region were taken
Literature	values found in the literature [e]...experimental [s]...simulated

	Properties	Surface/ Comment	$\overline{\sigma_{VM}}$ [GPa]	Literature σ_{VM}/GPa	$\overline{\sigma_{11}}$ [GPa]	XRD [GPa]	Literature σ_{XX}/GPa
Si Wafer	160x160 μm^2	min			-0.07		
		max	0.18		0.06		0.028[e][41]
		span	0.18		0.13		0.0015[e] [42]
		mean	0.08		0.008		0.00325[e][41]
WC	high magnetic saturation	ground	6.44		1.49	-1.806 ± 0.053	
		untreated	1.54	0.68[s][20]	0.27	-0.200 ± 0.036	-0.342 [s][43]
		centre	5.36		0.68		-0.283 ± 0.255[s][20]
	low magnetic saturation	ground	4.57		-0.29	-2.203 ± 0.077	
		untreated	1.38	0.68[s][20]	0.53	-0.363 ± 0.040	-0.342 [s][43]
		centre	5.51		0.12		-0.283 ± 0.255[s][20]
Co	high magnetic saturation	ground	4.23		-1.43		
		untreated	1.32	1.183[s][20]	0.09		0.935 ± 0.155 [s][20]
		centre	2.70		0.66		1.512 ± 0.266 [s][20]
	low magnetic saturation	ground	5.36		0.24		
		untreated	1.20	1.183 [s][20]	-0.20		0.935 ± 0.155 [s][20]
		centre	1.65		-0.63		1.512 ± 0.266 [s][20]

6 Conclusion and Outlook

6.1 Summary and Conclusion

The aim of this present work was to investigate the influence of surface treatment on stress levels in cemented carbides. The possibilities and reliability of the values of the CrossCourt 4.0 (CC4) software were evaluated. A calibration of the effective pixel size (section 3.5.2) and the fast Fourier transformation (FFT) (section3.5.4) parameters was carried out. A procedure for finding useful reference patterns was found (section 3.5.3). The stress levels were calculated with the CC4 software, which is based on the calculation of a cross correlation function (XCF). Further specific analyses were done with Matlab (section 3.5.5). Results of an x-ray diffraction (XRD) measurement of the samples were used to compare the EBSD with the well-established XRD method.

A silicon wafer and six tungsten-carbide cobalt (WC-Co) samples were examined to investigate the magnetic saturation influence on the residual stress levels and the surface treatment's influence on the stress levels. With the assumption of low stress levels within a silicon single crystal wafer, this sample served to answer the question on the calculated values' reliability. Within an area of $160x160$ μm^2 σ_{11} stress values between -0.07 GPa and 0.06 GPa were found. The maximum σ_{VM} value was calculated to 0.18 GPa.

The measurements of the WC-Co samples investigated the magnetic saturation's influence on the residual stress levels. A significant correlation could not be observed. Samples with high values for magnetic saturation release their stress by undergoing a phase transition from face centered cubic (fcc) to hexagonal closed pack (hcp). A correlation between surface treatment and stress was found directly at the ground

surface. Up to a depth of about one grain size, tungsten-carbide (WC) grains and cobalt (Co) grains from samples with ground surface showed significantly higher stress levels than samples with untreated surface. This stress also induces a phase transition for Co from fcc to hcp. The fcc Co binder phase consists of grains far larger than the occurring WC coarse grains. Measured areas of $20x20\ \mu m^2$ show just one single Co fcc grain.

EBSD in combination with CC4 is a powerful technique for localising type III mechanical stress within single grains. Investigations on a microscopic level and high local resolution are possible. The software offers the ability to execute orientation, stress and phase measurements. A wide range of properties are calculated by the CC4 software.

6.2 Outlook

6.2.1 Preparation

In order to get a surface without grooves, it is necessary to improve the preparation method. Possible are new blade materials with a better blade edge resulting in a protection of the sample edge as well as turning the sample to have more angles of attack for the ion and therefore smoother surface.

6.2.2 Comparison between XRD and EBSD Measurements

A reliable comparison between the well-established XRD method and the values obtained by the CC4 could not be obtained due to differences in the analysing method. While XRD yields type I stress values, which are an average value over a larger volume. EBSD analyses mechanical stress with a high local resolution within single grains known as type III

stress. This present work did not succeed with finding a quantitative comparison between these methods. A correlation going beyond qualitative comparisons would be preferable.

6.2.3 Absolute Values

For a better evaluation of the results knowing the absolute error is crucial. Investigations with a larger number of samples could give an estimation of the total error. Correlations between a force acting on a sample, and the measured stress could be obtained by bending a silicon (Si) wafer with a defined strength in a vise device. This would allow to introduce defined force into the sample and calculate the resulting stress. A comparison of the calculated and the measured stress is then possible.

Appendix

References

[1] P. J. Withers and H.K.D.H. Bhadeshia. "Residual stress. Part 1 – Measurement techniques". In: *Materials Science and Technology* 17.4 (2001), pp. 355–365. ISSN: 0267-0836. DOI: 10.1179/026708301101509980 (cit. on pp. 1, 13, 15).

[2] *Zeiss.at*. 2020-06-17T09:50:52.000Z. URL: https://www.zeiss.at/corporate/home.html (cit. on p. 3).

[3] Dominique Drouin et al. "CASINO V2.42: a fast and easy-to-use modeling tool for scanning electron microscopy and microanalysis users". In: *Scanning* 29.3 (2007), pp. 92–101. ISSN: 0161-0457. DOI: 10.1002/sca.20000 (cit. on p. 5).

[4] Anthony D. Rollett and Katayun Barmak. "Orientation Mapping". In: *Physical metallurgy*. Ed. by David E. Laughlin and Kazuhiro Hōno. Burlington: Elsevier Science, 2014, pp. 1113–1141. ISBN: 9780444537706. DOI: 10.1016/B978-0-444-53770-6.00011-3 (cit. on p. 6).

[5] Andreas Schreiber. "Ermittlung der Texturabhängigkeit elektrochemischer Eigenschaften von Eisen mit ortsaufgelösten Methoden". Dissertation. Düsseldorf: Heinrich-Heine-Universität, 2005. URL: https://docserv.uni-duesseldorf.de/servlets/DocumentServlet?id=3369 (cit. on p. 6).

[6] Valerie Randle. "Theoretical Framework for Electron Backscatter Diffraction". In: *Electron Backscatter Diffraction in Materials Science*. Ed. by Adam J. Schwartz, Mukul Kumar, and Brent L. Adams. Boston, MA: Springer, 2000, pp. 19–30. ISBN: 978-1-4757-3205-4. DOI: 10.1007/978-1-4757-3205-4{\textunderscore}2. URL: https://doi.org/10.1007/978-1-4757-3205-4_2 (cit. on p. 6).

[7] R. A. Schwarzer et al. *Present State of Electron Backscatter Diffraction and Prospective Developments*. 2008 (cit. on p. 6).

[8] C. Dresbach, M. Mittag, and M. Petzold. "Elastic properties of bonding wires". In: *3rd Electronic System-Integration Technology Conference (ESTC), 2010*. Piscataway, NJ: IEEE, 2010, pp. 1–4. ISBN: 978-1-4244-8553-6. DOI: 10.1109/ESTC.2010.5642992 (cit. on p. 7).

[9] *Thorlabs, Inc. - Your Source for Fiber Optics, Laser Diodes, Optical Instrumentation and Polarization Measurement & Control*. 2020-08-03T14:58:32.000Z (cit. on p. 6).

[10] *OIM Analysis™ — EDAX*. 2020-05-03T10:16:30.000Z. URL: https://www.edax.com/products/ebsd/oim-analysis (cit. on pp. 7, 19, 24).

[11] S. Zaefferer. "On the formation mechanisms, spatial resolution and intensity of backscatter Kikuchi patterns". In: *Ultramicroscopy* 107.2-3 (2007), pp. 254–266. ISSN: 0304-3991. DOI: 10.1016/j.ultramic.2006.08.007 (cit. on pp. 7, 8).

[12] S. Vespucci et al. "Digital direct electron imaging of energy-filtered electron backscatter diffraction patterns". In: *Physical Review B* 92.20 (2015), p. 738. ISSN: 1422-6375. DOI: 10.1103/PhysRevB.92.205301 (cit. on p. 8).

[13] Stuart I. Wright, Matthew M. Nowell, and David P. Field. "A review of strain analysis using electron backscatter diffraction". In: *Microscopy and microanalysis : the official journal of Microscopy Society of America, Microbeam Analysis Society, Microscopical Society of Canada* 17.3 (2011), pp. 316–329. DOI: 10.1017/S1431927611000055 (cit. on pp. 8–10).

[14] Rudolf Gross and Achim Marx. *Festkörperphysik*. 2., aktualisierte Aufl. De Gruyter Studium. Berlin and Boston: De Gruyter, 2014. ISBN: 3110358697. DOI: 10.1524/9783110358704. URL: https://www.degruyter.com/dg/page/e-books/ebooks (cit. on pp. 11, 12).

[15] Joachim Rösler, Harald Harders, and Martin Bäker. *Mechanisches Verhalten der Werkstoffe*. Wiesbaden: Springer Fachmedien Wiesbaden, 2019. ISBN: 978-3-658-26801-5. DOI: 10.1007/978-3-658-26802-2 (cit. on pp. 12, 14, 15).

[16] K. H. Kloos. “Eigenspannungen, Definition und Entstehungsursachen”. In: *Materialwissenschaft und Werkstofftechnik* 10.9 (1979), pp. 293–302. ISSN: 1521-4052. DOI: 10.1002/mawe.19790100906 (cit. on p. 12).

[17] U. Wolfstieg and E. Macherauch. “Ursachen und Bewertung von Eigenspannungen”. In: *Chemie Ingenieur Technik - CIT* 45.11 (1973), pp. 760–770. ISSN: 0009-286X. DOI: 10.1002/cite.330451103 (cit. on pp. 13, 14).

[18] Jun Jiang, T. Benjamin Britton, and Angus J. Wilkinson. “Mapping type III intragranular residual stress distributions in deformed copper polycrystals”. In: *Acta Materialia* 61.15 (2013), pp. 5895–5904. ISSN: 13596454. DOI: 10.1016/j.actamat.2013.06.038 (cit. on pp. 13, 75, 76).

[19] F. Cardarelli. *Materials Handbook: A Concise Desktop Reference*. Springer London, 2008. ISBN: 9781846286698. URL: https://books.google.at/books?id=PvU-qbQJq7IC (cit. on p. 14).

[20] Ji-fei Zhu et al. “Real microstructure-based simulation of thermal residual stresses in cemented carbides and the related strengthening and toughening consideration”. In: *International Journal of Refractory Metals and Hard Materials* 71 (2018), pp. 239–245. ISSN: 0263-4368. DOI: 10.1016/j.ijrmhm.2017.11.014 (cit. on pp. 14, 40, 77, 78).

[21] G. S. Schajer. “Residual Stresses: Measurement by Destructive Testing”. In: *Encyclopedia of materials*. Ed. by K. H. Jürgen Buschow. Amsterdam: Elsevier, 2001, pp. 8152–8158. ISBN: 978-0-08-043152-9. DOI: 10.1016/B0-08-043152-6/01462-5 (cit. on p. 15).

[22] P. J. Withers et al. “Recent advances in residual stress measurement”. In: *International Journal of Pressure Vessels and Piping* 85.3 (2008), pp. 118–127. ISSN: 03080161. DOI: 10.1016/j.ijpvp.2007.10.007 (cit. on p. 15).

[23] N. G. Ferreira et al. “Analysis of residual stress in diamond films by x-ray diffraction and micro-Raman spectroscopy”. In: *Journal of Applied Physics* 91.4 (2002), pp. 2466–2472. ISSN: 0040-6090. DOI: 10.1063/1.1431431 (cit. on p. 15).

[24] A. J. Wilkinson, G. Meaden, and D. J. Dingley. "High resolution mapping of strains and rotations using electron backscatter diffraction". In: *Materials Science and Technology* 22.11 (2006), pp. 1271–1278. ISSN: 0267-0836. DOI: 10.1179/174328406X130966 (cit. on pp. 16, 64).

[25] A. Steuwer et al. "High-resolution strain mapping in bulk samples using full-profile analysis of energy dispersive synchrotron X-ray diffraction data". In: *Nuclear Instruments and Methods in Physics Research Section B: Beam Interactions with Materials and Atoms* 238.1-4 (2005), pp. 200–204. ISSN: 0168583X. DOI: 10.1016/j.nimb.2005.06.049 (cit. on p. 16).

[26] *CrossCourt4 — HR-EBSD.com*. 2.3.2020. URL: http://www.hrebsd.com/wp/ (cit. on pp. 16, 17, 36, 37).

[27] Angus J. Wilkinson, Graham Meaden, and David J. Dingley. "High-resolution elastic strain measurement from electron backscatter diffraction patterns: new levels of sensitivity". In: *Ultramicroscopy* 106.4-5 (2006), pp. 307–313. ISSN: 0304-3991. DOI: 10.1016/j.ultramic.2005.10.001 (cit. on pp. 16, 64).

[28] Graham Meaden. *CrossCourt4 - User Guide: HR EBSD Based Starin Measurement Software*. Ed. by BLGVantage. User Guide. 2015 (cit. on p. 17).

[29] Z. Zak Fang et al. "Synthesis, sintering, and mechanical properties of nanocrystalline cemented tungsten carbide – A review". In: *International Journal of Refractory Metals and Hard Materials* 27.2 (2009), pp. 288–299. ISSN: 0263-4368. DOI: 10.1016/j.ijrmhm.2008.07.011 (cit. on p. 17).

[30] José García et al. "Cemented carbide microstructures: a review". In: *International Journal of Refractory Metals and Hard Materials* 80 (2019), pp. 40–68. ISSN: 0263-4368. DOI: 10.1016/j.ijrmhm.2018.12.004 (cit. on p. 17).

[31] Luxembourg CERATIZIT Luxembourg S.à r.l. Mamer. *Carbide Solutions. Carbide Producer & Manufacturer*. personal communication. 1.5.2020. URL: https://www.ceratizit.com/ (cit. on pp. 18, 59, 76, 78).

[32] Prakash LJ. *Weiterentwicklung von Wolframcarbid Hartmetallen unter Verwendung von Eisen-Basis-Bindelegierungen: Doctorate Thesis*. Karlsruhe, Germany, 1979 (cit. on p. 18).

[33] Zs Radi et al. "Surface polishing and slope cut by parallel ar ion beams for high resolution electron backscatter diffraction measurements". In: *2014 International Conference on Nanoscience and Nanotechnology (ICONN)*. Piscataway, NJ: IEEE, 2014, pp. 1–3. ISBN: 978-1-4799-3522-2. DOI: 10.1109/ICONN.2014.6965245 (cit. on p. 21).

[34] Robert A. Schwarzer. "Automated crystal lattice orientation mapping using a computer-controlled SEM". In: *Micron* 28.3 (1997), pp. 249–265. ISSN: 09684328. DOI: 10.1016/S0968-4328(97)00010-3 (cit. on p. 30).

[35] Robert Schwarzer. *Basics of EBSD and BKD*. 9.7.2019. URL: http://www.ebsd.info/basics.htm (cit. on p. 30).

[36] C. Moussa et al. "About quantitative EBSD analysis of deformation and recovery substructures in pure Tantalum". In: *IOP Conference Series: Materials Science and Engineering* 89 (2015), p. 012038. ISSN: 0965-0393. DOI: 10.1088/1757-899X/89/1/012038 (cit. on p. 36).

[37] K. P. Mingard et al. "Visualisation and measurement of hardmetal microstructures in 3D". In: *International Journal of Refractory Metals and Hard Materials* 71 (2018), pp. 285–291. ISSN: 0263-4368. DOI: 10.1016/j.ijrmhm.2017.11.023 (cit. on pp. 54, 70).

[38] S. Villert et al. "Accuracy assessment of elastic strain measurement by EBSD". In: *Journal of microscopy* 233.2 (2009), pp. 290–301. DOI: 10.1111/j.1365-2818.2009.03120.x (cit. on pp. 60, 64).

[39] Graham Meaden. *User Guide for the CrossCourt 3 Strain Measurement Tool*. Ed. by BLG Productions Ltd 2010. 2013 (cit. on p. 64).

[40] S. Karmakar et al. "Pressure-induced phase transitions in cobalt-filled multiwalled carbon nanotubes". In: *Physical Review B* 73.18 (2006), p. 78. ISSN: 1422-6375. DOI: 10.1103/PhysRevB.73.184119 (cit. on p. 71).

[41] Chris Yang et al. "On the residual stress and fracture strength of crystalline silicon wafers". In: *Applied Physics Letters* 102.2 (2013), p. 021909. ISSN: 0003-6951. DOI: 10.1063/1.4776706 (cit. on pp. 77, 78).

[42] *Measurement of residual stress in single crystal silicon wafers*. New York City, NY: IEEE, 2002, pp. 297–301. ISBN: 0-7803-7434-7. DOI: 10.1109/ISAPM.2002.990402 (cit. on pp. 77, 78).

[43] V. T. Golovchan. "On the thermal residual microstresses in WC–Co hard metals". In: *International Journal of Refractory Metals and Hard Materials* 25.4 (2007), pp. 341–344. ISSN: 0263-4368. DOI: 10.1016/j.ijrmhm.2006.08.002 (cit. on pp. 77, 78).